Mapping DFT to effective Hamiltonians

Department of Mathematical Physics
Lund University

Author : Paul André
Supervisor : Gillis Carlsson
Co-supervisor : Andrea Idini
Examiner : Jakob Bengtsson

Degree project submitted for the degree of
Master of Science in Engineering

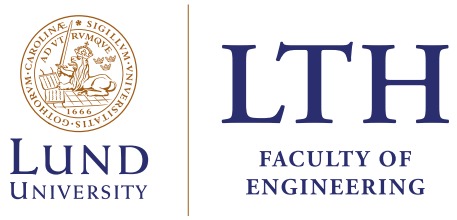

LTH Faculty of Engineering
Lund University
June 2019

Abstract

This thesis proposes a new effective Hamiltonian to represent the interactions taking place in the atomic nucleus. This estimated Hamiltonian is analogous to the Pairing-Plus-Quadrupole model and this work is focused exclusively on the quadrupole part, with the aim of describing nuclear structure in a computationally efficient way. We have compared the accuracy of our proposed expression with the one proposed by K. Kumar and B. Sørensen [Nucl. Phys. **A146** (1970) 1][1] studying the root-mean-squared error between those estimates and the exact formula. We also compare the spectra yielded by the different expressions. After this study, we conclude that the derived approximations appear to be more precise than the one proposed by Kumar and Sørensen.

Detta examensarbete föreslår en ny effektiv Hamiltonian för att representera fenomen i atomkärnor. Denna approximativa Hamiltonian är baserad på Parning-Plus-Kvadrupol-modellen och detta arbete fokuserar endast på kvadrupoldelen, med målet att ge en beskrivning av kärnstruktur på ett beräkningseffektivt sätt. Vi har jämfört precisionen av vår approximation med den av K. Kumar och B. Sørensen [Nucl. Phys. **A146** (1970) 1][1] genom att studera root-mean-squared-felet. Vi jämför också spektrerna svarande mot de olika uttrycken. Efter detta arbete är slutsatsen att approximationerna vi härlett är mer precisa än Kumar-Sørensen-ekvationerna.

Preface

This document is the report of my degree project at LTH Faculty of Engineering of Lund University. This thesis is the final assignment of a two-year Master's program in Engineering Physics, worth 30 credits over 120 for the whole program. My specialization in this program is Theoretical Physics, and as a consequence, the field concerned by this study is Theoretical Nuclear Physics. The work for this project has been performed in the course of six months, from January to June 2019, in the division of Mathematical Physics at the Faculty of Engineering in Lund University.

Before diving into nuclear physics, I would like to thank my supervisor, Gillis Carlsson, for his precious help, his patience and his very friendly attitude towards me all along this project. I also thank my co-supervisor, Andrea Idini, for his enthusiasm and his advice on nuclear physics. I would like to thank Philipp Stürmer, Erik Linnér and Tor Sjöstrand for their precious feedbacks that made my writing better. For his very careful review of this thesis, I warmly thank Jakob Bengtsson. I also thank and congratulate Carl Frostenson, Ingemar Ragnarsson and Gunnar Ohlén for coping with me as an office mate, and for providing a nice and friendly working environment during those six months. I will finally thank my family for their never-ending support throughout my studies, and Maitane who made my days at work brighter.

Contents

Introduction

The many-body problem is a broad ensemble of problems that can be summed up the following way : it is difficult (and sometimes impossible) to completely describe a system of several physical objects interacting with each other. As a consequence, there are several versions of the many-body problem, applied to different fields of physics. This work focuses on the nuclear many-body problem. Indeed, atomic nuclei are made of neutrons and protons interacting with each other mainly through the strong force and the Coulomb force. So in order to understand and represent this system, it is necessary to approach the quantum many-body problem. Density Functional Theory (DFT) and effective Hamiltonians are methods to tackle this, and are of central importance for the following work.

The aim of this thesis is to provide an accurate effective Hamiltonian. To do so, we will use an existing model and modify some of its features. We will then see to what extent those changes improve the existing model. With this improved version of the Hamiltonian, we expect to provide an efficient tool to compute the spectrum of atomic nuclei and provide precise information about the interaction in this system using affordable computer power.

In chapter 1, the effective Hamiltonian used in the thesis is introduced, as well as the proposed by Kumar and Sørensen in [1]. Chapter 2 will introduce the reasoning behind the different derivations of each expression, and the process that has been followed to compare them. The obtained results are presented and discussed in chapter 3, and a conclusion with outlooks is proposed in chapter 4.

Chapter 1

Theoretical background

1.1 Density Functional Theory (DFT)

DFT is a powerful tool used to describe numerous physical systems [2]. It relies, as its name indicates, on the particle density rather than on the potential to compute the wave function that represents the considered system. This approach is supported by the Hohenberg-Kohn theorem. This theorem, first derived by Pierre Hohenberg and Walter Kohn in 1964 [3], states that there exists a unique functional of the particle density of the system that provides the total energy of the system. So whereas the usual process is to use the interaction between particles and the Schrödinger equation to find the wave function of the system, the first step in DFT is to find the density of particles and then compute the ground state energy as a functional of the density, using the Hohenberg-Kohn theorem [2]. The Hohenberg-Kohn theorem being a very general result, DFT is a versatile method. One of the application of those results is the Kohn-Sham algorithm which is a self-consistent method used first in the case of inhomogeneous electron gases [4], and later applied to a wider range of problems. The very first ideas of such methods for nuclear physics, without naming them DFT, were initiated by the work of Tony Skyrme in 1959 [5]. More details about the Kohn-Sham equations and the Kohn-Sham algorithm can be found in appendix A.

1.2 Effective Hamiltonians

The idea underlying this thesis is to use DFT to calculate the stiffness of a nucleus with respect to perturbing fields and map to an effective Hamiltonian. On the one hand, the interaction between the nucleons represents the considered nucleus very accurately, but on the other hand, it is usually not simple and yields a complicated Hamiltonian. As a consequence, using it would lead to heavy computations. One alternative approach is to start with a simpler separable Hamiltonian that represents the effective interactions of the system and map this one to the corresponding DFT calculations. Behind those Hamiltonians are approximations that lower the number of parameters of the problem. In the following subsection, examples of effective Hamiltonians are given. We then focus on the Pairing-Plus-Quadrupole model, which provides the effective Hamiltonian we use in this thesis.

1.2.1 Particle-Vibration Coupling (PVC)

As stated previously, it is not possible to consider all nucleons and their different interactions to obtain the behavior of the system analytically. The PVC model, initially called the Bohr-Mottelson model from the name of the physicists who first proposed it, avoids considering every nucleon one by one and is rather based on their collective motion. This idea of collective motion has been first deduced studying the β-decay of a series of nuclei [6]. The main feature of the model is that it primarily considers the collective vibration of the whole atomic nucleus [7]. Indeed, the nucleus is considered as a whole and the vibration is described by parameterizing the radius [8]. This collective motion is then coupled with the single-particle moving in a mean field [8], resulting in mixing the collective and single-particle degrees of freedom. The corresponding Hamiltonian can then be divided in three terms : one for the surface collective motion, one for the particle levels and one for the coupling between both.

1.2.2 Interacting Bosons Approximation (IBA)

Another way to reduce the number of parameters of the problem is to represent the different particles in groups. This is the main principle of the IBA model. It indeed relies on the representation of a pair of fermions by a boson. The excitation of a large number of fermions and the excitation of a smaller number of bosons are very similar [9]. It has been proved that they define the same mathematical structure by Akito Arima and Francesco Iachello in 1975 [10]. This way, the number of particles to treat decreases drastically, simplifying the representation of the problem.

Both PVC and IBA have been widely used during the past decades and have been proven to give satisfactory results [11]. However, those methods still struggle to represent certain specific nuclei, with an odd number of particles or with a single particle on the last level after a closed shell for instance [11]. The starting point of this work is another effective Hamiltonian that comes from the Pairing-Plus-Quadrupole model.

1.3 The Pairing-Plus-Quadrupole interaction

The Pairing-Plus-Quadrupole interaction is a model used to describe nucleonic interactions in an atomic nucleus. This tool has been extensively studied by L. Kisslinger and R. Sorensen [12] and has been built by adding corrections to an average spherical single-particle potential for quadrupole deformations of the mean field and for the pairing interaction (hence its name). This work is focused on the quadrupole deformation term.

1.3.1 The Pairing-Plus-Quadrupole Hamiltonian

It appears that two interactions are of particular importance in the atomic nucleus, in addition to the single-particle potential. One of them is a correlation phenomenon due to the deformation of the mean field, the other is due to pairing. Consequently, the form of

the Hamiltonian is the following one (from [13] eq. (7.61)),

$$H = \sum_k \epsilon_k c_k^+ c_k - \frac{1}{2}\chi \sum_{\mu=-2}^{2} : Q_\mu^+ Q_\mu : -GP^+P, \tag{1.1}$$

with,

$$Q_\mu = \sum_{kk'} \langle k| \, P(r) Y_{2\mu} \, |k'\rangle \, c_k^+ c_{k'}. \tag{1.2}$$

The notation using the colons $: \cdot :$ refers to the normal ordering operator. The operators c_k and c_k^+ are respectively the creation and annihilation operators corresponding to the single-particle energy ϵ_k in the second quantization formalism. The parameter χ is the strength coefficient of the interaction. The $Y_{2\mu}$ functions correspond to the set of the spherical harmonics for which $l = 2$ and $\langle k|$ and $|k'\rangle$ are both arbitrary states. The radial function $P(r)$ is called the form factor.

This Hamiltonian is the sum between the interaction of particles in a spherical single-particle potential (first sum), a deformation interaction (second sum) and a pairing term (last term). One can simplify the previous equation in the Hartree-Fock-Bogoliubov (HFB) approximation ([13] eq. (7.64)). Dropping the pairing term (that is not going to be treated in this thesis), we have the following Hamiltonian,

$$H_{HFB} = \sum_k \epsilon_k c_k^+ c_k - \frac{1}{2}\chi \sum_{\mu=-2}^{2} \langle Q_\mu \rangle (Q_\mu^+ + Q_\mu). \tag{1.3}$$

The HFB approach linearize the Hamiltonian. With this linear quadrupole operator, one usually uses a form factor that originates from the modified harmonic oscillator potential, or Nilsson potential [14]. This form for the potential has the advantage to be exactly solvable. Furthermore, it yields a Nilsson potential as a mean field [15]. However, the Nilsson potential does not entirely represent the physics of the system. This potential has a parabolic shape and diverges as one goes away from the center of the nucleus, giving the interaction an infinite range. To have a model that is closer to reality, one can use a potential with a finite range. The one considered here is the Woods-Saxon potential. We then assume that the single-particle term of the Hamiltonian has the shape of a spherical Woods-Saxon potential. As a consequence, the form factor should represent the quadrupole deformation of this potential.

1.3.2 Using a Woods-Saxon mean field

We use here an analogous reasoning as the one presented in the previous section. We consider a new Hamiltonian for the Pairing-Plus-Quadrupole model,

$$\tilde{H} = \sum_k \widetilde{\epsilon_k} \widetilde{c_k}^+ \widetilde{c_k} - \frac{1}{2}\chi \sum_{\mu=-2}^{2} \langle \widetilde{Q_\mu} \rangle (\widetilde{Q_\mu}^+ + \widetilde{Q_\mu}). \tag{1.4}$$

We have here already dropped the pairing term that is not in the scope of this thesis. Here, the operators have the same physical meaning as the one before but do not have the same form. As stated in subsection 1.3.1, the first sum has the shape of a deformed

Woods-Saxon potential. For the form factor $P(r)$, we consider first a potential proposed by K. Kumar and B. Sørensen in [1]. The idea of Kumar and Sørensen is to propose a first-order Taylor expansion over the radius parameter r of a deformed Woods-Saxon potential to which a Coulomb and a spin-orbit term have been added.

$$\begin{aligned} V(r) = W_\tau &\left(f(r) - r\beta_2 Y_{20}(\theta)\frac{\partial f(r)}{\partial r} \right) \\ &+ \frac{1}{2}(1-\tau)\left(H_C(r) - r\beta_2 Y_{20}(\theta)\frac{\partial H_C(r)}{\partial r} \right) \\ &- \frac{1}{2}W_\tau v_{s-o}\lambda^2 \left(-(\mathbf{p}\times\mathbf{s})\cdot\nabla f(r) + \beta_2 Y_{20}(\theta)\frac{\partial^2 f(r)}{\partial r^2}\mathbf{l}\cdot\mathbf{s} \right), \end{aligned} \tag{1.5}$$

with

$$\begin{aligned} f(r) &= \frac{1}{1+\exp(\frac{r-R_0}{a})}, \\ H_C(r) &= Ze^2\left(\frac{1}{r}\Theta(r-R_c) + \frac{1}{R_c}\left(\frac{3}{2} - \frac{1}{2}\left(\frac{r}{R_c} \right)^2 \right)\Theta(R_c - r) \right), \\ W_\tau &= V_0 + V_1\frac{\mathbf{t}\cdot\mathbf{T}}{A}, \\ \lambda &= \frac{\hbar}{Mc}\left(1 + \frac{1}{A} \right). \end{aligned}$$

In this expression, r and θ are respectively the radial and polar parameter in spherical coordinates. The spherical Woods-Saxon potential is given by $f(r)$. W_τ is the strength of this interaction. The term $V_1\frac{\mathbf{t}\cdot\mathbf{T}}{A}$ makes this factor different for protons and neutrons. We consider in the following work that $W_\tau = V_0$. A and Z are respectively the mass and charge number of the considered nucleus. H_C is an approximation of the Coulomb potential proposed by Kumar and Sørensen, where e is the elementary charge, R_c the characteristic radius of the charge distribution, and Θ the Heaviside function. The prefactor $\frac{1}{2}(1-\tau)$, with τ the isospin of the nucleons, ensures that the Coulomb potential is only considered for protons. $\tau = -1$ for protons and $\tau = 1$ for neutrons, in which case the prefactor cancels. M is the nucleonic mass, and c the speed of light.

The procedure described in [1] to extract the form factor from this potential consists in keeping the radial function that is multiplied by Y_{20}. This yields the following form factor,

$$P_{KS}(r) = W_\tau r\frac{\partial f(r)}{\partial r} + \frac{1}{2}(1-\tau)r\frac{\partial H_C(r)}{\partial r} - \frac{1}{2}W_\tau v_{s-o}\lambda^2\frac{\partial^2 f(r)}{\partial r^2} \tag{1.6}$$

Using this form factor is not as mathematically satisfactory as using the Nilsson potential, for the Hamiltonian is not analytically solvable anymore. However, this potential takes into account more physics than the modified harmonic oscillator and the interaction has now a finite range. The objective in the next chapter is to try to improve and refine the form factor proposed in [1] to have a more accurate quadrupole interaction.

Chapter 2

Methodology

The goal of this thesis is to refine equation (1.6) provided by Kumar and Sørensen by proposing a different deformed Woods-Saxon potential. This chapter's main purpose is then to set and present the different approximations that we propose to improve each term of the potential, given by equation (1.5). Their precision will then be compared and evaluated in chapter 3.

2.1 The Woods-Saxon term

The spherical Woods-Saxon nuclear potential is the following one,

$$V_N(r) = \frac{W_\tau}{1+\exp(\frac{r-R_0}{a})} = W_\tau f(r), \tag{2.1}$$

with a the diffuseness of the potential and R_0 the characteristic radius of the nuclear mass distribution. First, we need to insert deformations in this spherical Woods-Saxon potential. To do so, we first consider the following parameterization for the radius of the deformed nucleus (from [16] eq. (6.52)),

$$R(\theta) = R_0\left(1+\sum_{n=2}^{N}\beta_n Y_{n0}(\theta) - \frac{\beta_n^2}{4\pi}\right). \tag{2.2}$$

Now dropping the second order term in β^2 and keeping the quadrupole deformations only, the deformed radius becomes,

$$R(\theta) \simeq R_0(1+\beta_2 Y_{20}(\theta)) \tag{2.3}$$

We insert this formula for the radius into the previous spherical potential, and assume, that the angular part of this potential can be expanded over the basis of the spherical harmonics, using the completeness relation,

$$V_{exact}(\mathbf{r}) = \frac{W_\tau}{1+\exp(\frac{r-R_0(1+\beta_2 Y_{20}(\theta))}{a})} = W_\tau f(r) + \sum_{l>0}\beta_l Y_{l0}(\theta) f_{l,ex}(r). \tag{2.4}$$

To compare our approximations efficiently with the exact potential, we need to have similar shapes for all the expressions. The desired shape consists in a spherical term

(given by V_N) summed to a second term accounting for the deformations. Therefore, we project the expression on the Y_{20} spherical harmonics and compare the coefficient in front of this quadrupole deformation term,

$$V_{proj}(\mathbf{r}) = W_\tau f(r) + \beta_2 Y_{20}(\theta) f_{2,ex}(r, \beta_2). \tag{2.5}$$

We can then compute the coefficient $f_{2,ex}(r, \beta_2)$ by the following formula,

$$\begin{aligned} f_{2,ex}(r, \beta_2) &= \frac{1}{\beta_2} \iint Y_{20}(\theta)^* V_{exact}(\mathbf{r}) d\Omega \\ &= \frac{1}{\beta_2} \iint Y_{20}(\theta)^* \frac{W_\tau}{1 + \exp(\frac{r-R_0}{a}) \exp(\frac{-R_0 Y_{20}(\theta)\beta_2}{a})} d\Omega \\ &= \frac{2\pi}{\beta_2} \int_0^\pi Y_{20}(\theta) \sin(\theta) \frac{W_\tau}{1 + \exp(\frac{r-R_0}{a}) \exp(\frac{-R_0 Y_{20}(\theta)\beta_2}{a})} d\theta. \end{aligned} \tag{2.6}$$

The approximation in [1] is given by,

$$\begin{aligned} V_{N,KS}(\mathbf{r}) &= V_N(r) - \beta_2 Y_{20}(\theta) r \frac{\partial V_N(r)}{\partial r} \\ &= \frac{W_\tau}{1 + \exp(\frac{r-R_0}{a})} - \beta_2 Y_{20}(\theta) r \frac{W_\tau}{a(2 + \exp(\frac{r-R_0}{a}) + \exp(\frac{R_0-r}{a}))} \\ &= V_N(r) - \beta_2 Y_{20}(\theta) f_{N,KS,2}(r). \end{aligned} \tag{2.7}$$

This approximation is a Taylor expansion over r of V_{exact}. We propose to compare it with a Taylor expansion over the deformation parameter β_2,

$$\begin{aligned} V_{N,T}(\mathbf{r}) &= V_N(r) - \beta_2 \left. \frac{\partial V_{exact}(\mathbf{r})}{\partial \beta_2} \right|_{\beta_2=0} \\ &= \frac{W_\tau}{1 + \exp(\frac{r-R_0}{a})} - \beta_2 \frac{R_0 Y_{20}(\theta) W_\tau}{a(2 + \exp(\frac{r-R_0}{a}) + \exp(\frac{R_0-r}{a}))} \\ &= V_N(r) - \beta_2 Y_{20}(\theta) f_{N,T,2}(r). \end{aligned} \tag{2.8}$$

After settling these expressions, one can wonder why we consider $V_{N,T}$ and $V_{N,KS}$ while V_{proj} is closer to the exact potential and has the desired shape (a spherical term summed with a deformed term). We will see in section 2.4 later in this chapter that further computations require the deformation term to be separable, i.e. have a function of r multiplied with a functoin of θ. Unfortunately, $f_{2,ex}$ mixes both parameters and is not suitable for further computations.

2.2 The Coulomb term

This part deals with the Coulomb term of equation (1.5). This term is defined the following way,

$$V_{C,KS}(r) = H_C(r) = \frac{Ze^2}{4\pi\epsilon_0} \left(\frac{1}{r} \Theta(r - R_c) + \frac{1}{R_c} \left(\frac{3}{2} - \frac{1}{2} \left(\frac{r}{R_c} \right)^2 \right) \Theta(R_c - r) \right). \tag{2.9}$$

We remove the pre-factor depending on τ, assuming that we consider protons and that it is relevant to consider the Coulomb interaction. The method used to find a suitable approximation for this term is very similar to the one used in the previous section for the nuclear potential. However, we will use other expressions and other types of approximation here. Indeed, we have noted that the Taylor expansion on β_2 that has been performed in the previous paragraph is not efficient for the Coulomb term, for :

- The Coulomb interaction written this way (using the H_C function) is valid only under certain symmetries that the foreseen Taylor expansion does not preserve.
- Expanding over the deformations of the nucleus is not relevant for part of the Coulomb interaction is defined inside the surface of the nucleus, where the deformations only have a small impact.

2.2.1 The exact potential

We will first detail the derivation of the expression that we will consider as the one representing the exact Coulomb potential. The first step is to consider a density of protons with a Woods-Saxon shape,

$$\rho(\mathbf{r}) = \frac{N(\beta_2)}{1 + \exp(\frac{r - R_0(1+\beta_2 Y_{20}(\theta))}{a})}. \tag{2.10}$$

We have used the same parameterization for the radius as a function of θ as before (equation (2.2)). N is a normalization constant defined by the following constraint,

$$\iiint \rho(\mathbf{r}) d^3\mathbf{r} = Z, \tag{2.11}$$

with Z the charge number of the considered nucleus. We then have,

$$N(\beta_2) = \frac{Z}{2\pi} \left(\int_0^{\theta} \int_0^{\infty} \frac{r^2 \sin(\theta)}{1 + \exp(\frac{r - R_0(1+\beta_2 Y_{20}(\theta))}{a})} dr d\theta \right)^{-1}. \tag{2.12}$$

We define the Coulomb potential the following way,

$$V_C(\mathbf{r}') = \frac{e^2}{4\pi\epsilon_0} \iiint \frac{\rho(\mathbf{r})}{\mid \mathbf{r} - \mathbf{r}' \mid} d^3\mathbf{r}. \tag{2.13}$$

In that case, the expansion over the spherical harmonics is slightly more natural than in the other cases. To do so, we replace the difference between the two vectors in the denominator by its expansion over the spherical harmonics ([17], equation 5.17.4.21),

$$\frac{1}{\mid \mathbf{r} - \mathbf{r}' \mid} = \frac{4\pi}{r'} \sum_{l=0}^{\infty} \frac{1}{2l+1} \left(\frac{r}{r'}\right)^l \left(\sum_{m=-l}^{l} Y_{lm}^*(\Omega) Y_{lm}(\Omega') \right), \text{ for } r < r'. \tag{2.14}$$

We note here that the formula change depending on the sign of the difference. As stated in [17], the same expansion for $r' < r$ is obtained by interchanging r and r' in equation

(2.14). When inserting equation (2.14) into equation (2.13), one has to be careful about splitting the integral accordingly. This yields,

$$V_C(\mathbf{r}') = \frac{e^2}{4\pi\epsilon_0}\sum_{l,m}\left[\frac{4\pi}{2l+1}\frac{1}{r'^{l+1}}Y_{lm}(\Omega')I_{inf,l,m} + \frac{4\pi}{2l+1}r'^{l}Y^*_{lm}(\Omega')I_{sup,l,m}\right], \tag{2.15}$$

with :

$$I_{inf,l,m} = \int_0^{2\pi}\int_0^{\pi}\int_0^{r'} r^{l+2}\sin(\theta)\rho(\mathbf{r})Y^*_{lm}(\Omega)drd\theta d\varphi, \tag{2.16}$$

$$I_{sup,l,m} = \int_0^{2\pi}\int_0^{\pi}\int_{r'}^{\infty} r^{1-l}\sin(\theta)\rho(\mathbf{r})Y_{lm}(\Omega)drd\theta d\varphi. \tag{2.17}$$

It is interesting to remark that the coefficients $I_{inf,l,m}$ and $I_{sup,l,m}$ still depend on r' and are valid for any density. In the same fashion as previously, we approximate the whole sum to the sum between the monopole and the quadrupole term. We obtain the coefficient of the quadrupole term (dependent on r here as well) with the same process as in section 2.1. The spherical harmonics are orthonormal,

$$\iint Y_{lm}(\Omega)Y^*_{l'm'}(\Omega)d\Omega = \delta_{ll'}\delta_{mm'}. \tag{2.18}$$

This property drastically simplifies the expressions. To be able to compare equation (2.15) with the other approximations and to remain in the frame of the Pairing-Plus-Quadrupole interaction, we will project on the monopole and quadrupole terms of the expansion. With notations that are analogous with the previous part, this yields,

$$V_{C,proj}(\mathbf{r}') = Y_{00}(\theta')g_0(r',\beta_2) + \beta_2 Y_{20}(\theta')g_2(r',\beta_2). \tag{2.19}$$

This equation is slightly different from the one for the nuclear potential term for we cannot have radial functions multiplied by β_2. However, g_0 and g_2 are determined the same way as before,

$$g_0(r',\beta_2) = \iint Y^*_{00}(\theta')V_C(\mathbf{r}')d\Omega' = \frac{e^2}{4\pi\epsilon_0}4\pi(\frac{1}{r'}I_{inf,0,0} + I_{sup,0,0}), \tag{2.20}$$

$$g_2(r',\beta_2) = \frac{1}{\beta_2}\iint Y^*_{20}(\theta')V_C(\mathbf{r}')d\Omega' = \frac{e^2}{4\pi\epsilon_0}\frac{4\pi}{5}(\frac{1}{r'^3}I_{inf,2,0} + r'^2 I_{sup,2,0}), \tag{2.21}$$

with

$$I_{inf,0,0} = 2\pi\int_0^{\pi}\int_0^{r'} r^2\sin(\theta)\rho(\mathbf{r})Y_{00}drd\theta, \tag{2.22}$$

$$I_{sup,0,0} = 2\pi\int_0^{\pi}\int_{r'}^{\infty} r\sin(\theta)\rho(\mathbf{r})Y_{00}drd\theta, \tag{2.23}$$

$$I_{inf,2,0} = 2\pi\int_0^{\pi}\int_0^{r'} r^4\sin(\theta)\rho(\mathbf{r})Y_{20}(\theta)drd\theta, \tag{2.24}$$

$$I_{sup,2,0} = 2\pi\int_0^{\pi}\int_{r'}^{\infty}\frac{\sin(\theta)}{r}\rho(\mathbf{r})Y_{20}(\theta)drd\theta. \tag{2.25}$$

Now that those equations have been set, it is important to make sure that the potentials that are being compared are exactly equal in the spherical case, i.e. when $\beta_2 = 0$. To guarantee that, we set the monopole term to $g_0(r',0)$. We now build the quadrupole term for the two approximations that we will compare :

- The expansion made by Kumar and Sørensen
- An approximation made on the density of charge.

2.2.2 The Kumar-Sørensen expansion

The expansion used in [1] is a Taylor expansion on r of equation (2.9). The quadrupole term reads,

$$\begin{aligned} g_{2,KS}(r) &= -r\frac{\partial H_C(r)}{\partial r} \\ &= \frac{Ze^2r^2}{4\pi\epsilon_0 R_0^3}\theta(R_0 - r) + \frac{Ze^2}{4\pi\epsilon_0 r}\theta(r - R_0). \end{aligned} \tag{2.26}$$

The complete approximation is then,

$$V_{C,KS}(\mathbf{r}) = Y_{00}(\theta)g_0(r,0) + \beta_2 Y_{20}(\theta)g_{2,KS}(r). \tag{2.27}$$

2.2.3 The approximation on the density

This approximation relies on an expansion on the density rather than an expansion on the potential. With this approximated density, the derivation of the potential is very similar to the one conducted for the exact potential. The proposed expansion for the density is,

$$\rho(\mathbf{r}) = \rho^{(0)}(r) + \beta_2\rho^{(2)}(r)Y_{20}(\theta). \tag{2.28}$$

The function used for $\rho^{(0)}$ has a Woods-Saxon shape,

$$\rho^{(0)}(r) = \left.\frac{N(\beta_2)}{1 + \exp(\frac{r - R_0(1+\beta_2 Y_{20}(\theta))}{a})}\right|_{\beta_2=0} = \frac{N(0)}{1 + \exp(\frac{r-R_0}{a})}. \tag{2.29}$$

The normalization factor is the same as the one for the exact potential applied for $\beta_2 = 0$. This expansion is a Taylor expansion over the deformation parameter β_2. As a consequence, the shape of the deformed density is the derivative of the Woods-Saxon potential,

$$\rho^{(2)}(r) = \frac{N(0)R_0}{a(\exp(\frac{r-R_0}{a}) + \exp(\frac{R_0-r}{a}) + 2)}. \tag{2.30}$$

This gives rise to a potential composed of two parts,

$$\begin{aligned} V_{C,D}(\mathbf{r}') &= \frac{e^2}{4\pi\epsilon_0}\iiint \frac{\rho(\mathbf{r})}{|\ \mathbf{r} - \mathbf{r}'\ |}d^3\mathbf{r} \\ &= \frac{e^2}{4\pi\epsilon_0}\left(\iiint \frac{\rho^{(0)}(r)}{|\ \mathbf{r} - \mathbf{r}'\ |}d^3\mathbf{r} + \beta_2\iiint \frac{\rho^{(2)}(r)Y_{20}(\theta)}{|\ \mathbf{r} - \mathbf{r}'\ |}d^3\mathbf{r}\right). \end{aligned} \tag{2.31}$$

As we set the monopole term to $g_0(r',0)$, we can drop the monopole term in the previous expression (that is equal to $g_0(r',0)$ up to a constant anyway) and focus on the quadrupole term. Equation (2.14) and equation (2.18) can be used again to provide simpler expressions. We have,

$$g_{2,D}(r') = \frac{e^2}{4\pi\epsilon_0}\frac{4\pi}{5}\left(\frac{1}{r'^3}\int_0^{r'} r^4\rho^{(2)}(r)dr + r'^2\int_{r'}^{\infty}\frac{1}{r}\rho^{(2)}(r)dr\right). \tag{2.32}$$

Eventually, the potential using the expansion over the density reads,

$$V_{C,D}(\mathbf{r}') = g_0(r',0) + \beta_2 Y_{20}(\theta')g_{2,D}(r'). \tag{2.33}$$

2.3 The spin-orbit term

Treating the spin-orbit interaction is more difficult than treating the other terms of the effective Hamiltonian. In the previous sections, we could compare directly the different proposed expressions for they depended only on spatial coordinates. Their shape was the only important aspect to take care of. The spin-orbit interaction depends, as its name indicates it, on the considered orbital and on the spin of the nucleons, making it state-dependent. It is then necessary to consider a precise existing nucleus for the way the states are occupied is now an important information. As this interaction has a smaller impact than the other ones, and as we will compare the proposed expressions for the Woods-Saxon and Coulomb terms to the deformation factor in [1], we will here keep the same formula for the spin-orbit interaction as in [1], but we drop the term that depends on the Y_{10} spherical harmonics. The expression finally reads,

$$V_{SOKS}(\mathbf{r}) = \frac{1}{2} W_\tau v_{so} \lambda^2 \left(-(\mathbf{p} \times \mathbf{s}) \cdot \nabla f(r) + \beta_2 Y_{20}(\theta) \frac{\partial^2 f(r)}{\partial r^2} \mathbf{l} \cdot \mathbf{s} \right). \tag{2.34}$$

For further explanations about the treatment of the spin-orbit interaction in [1], a detailed derivation of this expression is presented in appendix B.

2.4 The contribution of each term

In the previous sections and subsections, the different physical phenomena that are taken into account in equation (1.5) have been treated separately. Different expressions have been derived for each interaction. The next step is then to analyze the contribution of each term within the total formula, but also to compare the Hamiltonian this yields with other Hamiltonians from other models.
In that case, Hamiltonians will be objects that are very convenient to use. Indeed, choosing a correct basis, one can directly access to their matrix elements, and then diagonalize the Hamiltonian matrix to have the spectrum of the considered nucleus. We then compare those spectra and plot the energy levels as functions of the deformation using the β parameter.
We first use the WSBETA code [19] (in *Fortran 77*) to provide the spectrum for a nucleus under an axially deformed Woods-Saxon potential. In this program, deformation are directly implemented in the potential in a similar way as the one shown before in equation (2.4),

$$V(\mathbf{r}, \hat{\beta}) = \frac{V_0}{1 + \exp(\frac{dist_\Sigma(\mathbf{r}, \hat{\beta})}{a})}, \tag{2.35}$$

with Σ being the surface of the nucleus, and,

$$\hat{\beta} = (\beta_2, \beta_3, \beta_4, \beta_5, \beta_6), \tag{2.36a}$$

$$dist_\Sigma(\mathbf{r}, \hat{\beta}) = r - c(\hat{\beta}) R_0 [1 + \sum_\lambda \beta_\lambda Y_{\lambda 0}(\cos\theta)]. \tag{2.36b}$$

This then provides the energy levels of the system in ascending order as an output, but also considers higher orders than quadrupole for the deformations. To remain in the scope of the quadrupole deformations, only β_2 is kept non-zero.

The corrections previously derived are added to a code named HOSPHE [20] (in *Fortran 90*). This program provides the matrices of the desired operators. Provided a basis of states $\phi_{nLM} = R_{nL}(r)Y_{LM}(\theta,\varphi)$ and an operator with the shape $A = f(r)Y_{L''M''}(\theta,\varphi)$, it computes,

$$\langle \phi_{n'L'M'} | A | \phi_{nLM} \rangle = \int R^*_{n'L'} f(r) R_{nL} r^2 dr \times \iint Y^*_{L'M'} Y_{L''M''} Y_{LM} \sin\theta d\theta d\varphi. \tag{2.37}$$

The angular integral can be computed rather simply using the addition theorem, merging two spherical harmonics into a sum of spherical harmonics weighted by the Clebsch-Gordan coefficients. The radial part is computed in the code using the Gauss-Hermite quadrature, the R_{nL} functions having Gaussian shapes. We then compute the matrix elements using the terms derived in section 2.1 and 2.2.
The Hamiltonian computed by WSBETA is,

$$H_{WSB} = T + V_{defWS} + \frac{1}{2}(1-\tau)V_{defC} + V_{so}, \tag{2.38}$$

with T the kinetic energy operator,

$$T = \frac{\mathbf{p}^2}{2M}. \tag{2.39}$$

The Hamiltonian computed by HOSPHE is the one that we build with the most efficient approximations derived in section 2.1 and 2.2. It has the following form,

$$H_{HOSPHE} = T + V_{sphWS} + \frac{1}{2}(1-\tau)V_{sphC} + \beta_2(V_{defWS}(r) + V_{defC}(r) + V_{so}). \tag{2.40}$$

The index *def* refers to the deformed version of the formula for the potential (either Coulomb with *C* or Woods-Saxon with *WS*) while the index *sph* refers to the formula in the spherical case. The index *so* stands for *spin-orbit*. For H_{WSB}, the deformations are directly included in the different potentials, while the potentials used in H_{HOSPHE} only depend on the radius (in an analogous way as the form factor defined in [1]) and are then multiplied by the deformation factor.
Provided that the diffuseness, the radius parameters and the depth of the potential are the same for both programs, it is possible to first compare the results yielded by both codes for a spherical and axially deformed Woods-Saxon potential (even though the used formulas are the same, the results can slightly differ, due to the fact that the integrals are numerically calculated). We can then use the output of each program to visualize on the spectrum :

- The contribution of each term with respect to the deformed Woods-Saxon term only.
- The contribution of each term with respect to all the interactions, i.e. Woods-Saxon, Coulomb and spin-orbit.

Chapter 3

Results and discussion

3.1 Comparing the different estimates

After setting up all the expressions for the different term of equation (1.5), we can eventually properly compare the different approximations proposed earlier. All this has then been implemented in *Python*. To apply the previous results, it is necessary to choose a precise nucleus on which the calculations will be performed. For the following computations, the chosen nucleus is ${}^{56}_{28}\mathrm{Ni}_{28}$. As far as numerical values are concerned, we compute R_0 using [14],

$$R_0 = r_0 A^{\frac{1}{3}}, \tag{3.1}$$

with r_0= 1.2 fm and A the mass number. This gives $R_0 \simeq$4.59 fm. We set a =0.57 fm for the diffuseness [14], and the depth of the potential $W_\tau = -49.6$ MeV [19].

To compare the Kumar-Sørensen formula for the Woods-Saxon term (Eq. (2.7)) and the proposed expansion (Eq. (2.8)) with the projected potential (Eq. (2.6)), we use the root-mean-squared (RMS) error between both expressions. For the following expression of the RMS error (denoted γ here), we consider an array $\vec{r}$ of length η to represent the continuous parameter r. This yields the following equations,

$$\gamma_{KS} = \sqrt{\frac{1}{\eta}\sum_{i=1}^{\eta}(V_{proj}(r_i,\theta_0,\beta_2) - V_{N,KS}(r_i,\theta_0,\beta_2))^2}, \tag{3.2}$$

$$\gamma_{T} = \sqrt{\frac{1}{\eta}\sum_{i=1}^{\eta}(V_{proj}(r_i,\theta_0,\beta_2) - V_{N,T}(r_i,\theta_0,\beta_2))^2}. \tag{3.3}$$

We have set θ to a constant value θ_0 to compare the radial part of each expression. Because of the way we constructed the term in equation (2.6), the RMS error depends in both cases on β_2. We then plot the error as a function of β_2. The approximation providing the smallest error is considered more accurate than the other.
In the particular case of the Woods-Saxon term, all compared expressions are the same for $\beta_2 = 0$. It is then possible to also consider the RMS error of those first order terms. Equations (3.2) and (3.3) then transforms in the following way, to see how the terms of

the expansion evolve with respect to the exact decomposition,

$$\gamma_{KS}^{(2)} = \sqrt{\frac{1}{\eta}\sum_{i=1}^{\eta}(f_{2,ex}(r_i,\beta_2) - f_{N,KS,2}(r_i))^2}, \tag{3.4}$$

$$\gamma_{T}^{(2)} = \sqrt{\frac{1}{\eta}\sum_{i=1}^{\eta}(f_{2,ex}(r_i,\beta_2) - f_{N,T,2}(r_i))^2}. \tag{3.5}$$

The points in $\vec{r}$ are equally spaced in every computations. For the RMS error on the Woods-Saxon potential, we set $\eta = 800$ and the range of values for r goes from 0 fm to $2R_0$ fm. For the RMS error on the Coulomb potential, we have $\eta = 300$ and the range of values r goes from 0 to 12 fm.

3.1.1 The Woods-Saxon term

Comparison using the RMS error

We compare the exact Woods-Saxon expansion (Eq. (2.4)) and the projected one (Eq. (2.5)), with the one obtained using the proposed Taylor expansion (Eq. (2.8)) and the formula proposed by Kumar and Sørensen [1] using the RMS errors for the first order terms using equations (3.4) and (3.5), and for the whole potential using equations (3.2) and (3.3).

In figure 3.1, we can first see the difference between both estimates and the projection as functions of the radius on the following plot for $\beta_2 = 0.2$ and $\theta = 0$. To have a more global view of the look of those potentials, 3D plots for the whole range of θ values are provided in appendix C. To observe more clearly how those expansions act on the deformed Woods-Saxon potential, figure 3.2 shows the first order terms $f_{2,ex}$, $f_{N,KS,2}$ and $f_{N,T,2}$ as functions of the radius.

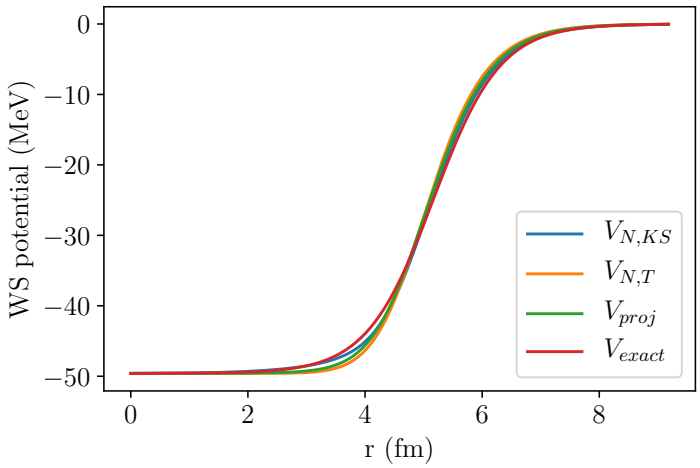

Figure 3.1: Deformed Woods-Saxon potential as a function of the radius computed in the case of ^{56}Ni. The blue line corresponds to the potential as computed in [1], the orange line corresponds to equation (2.8), the green one to the projected potential, and the red one to the exact potential, for the particular value $\beta_2 = 0.2$ and $\theta = 0$.

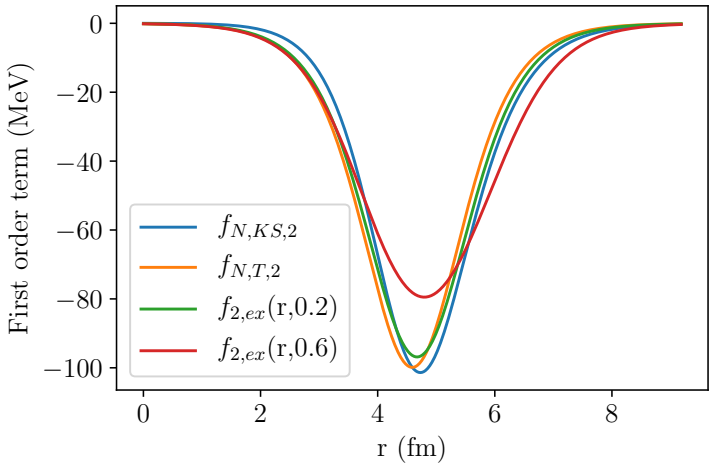

Figure 3.2: First order terms as a function of radius computed in the case of ^{56}Ni. The blue line corresponds to the first order term from [1], the orange line corresponds to the first order term of the Taylor expansion over β_2, the green one to the first order term of the projection for $\beta_2 = 0.2$, and the red one to the first order term of the projection for $\beta_2 = 0.6$.

We can see that, as the deformation increases, the bell goes lower and broader at its base. The approximations do not depend on β_2 and as a consequence, the curve remains the same. This explains part of the behavior of the RMS errors shown in figure 3.3 and 3.4.

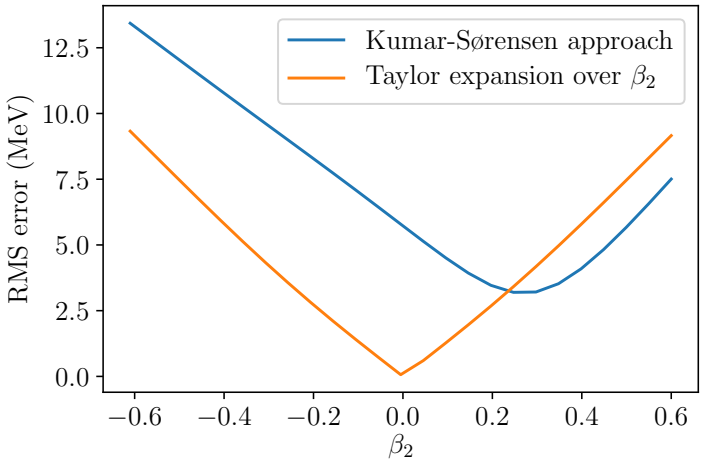

Figure 3.3: RMS error of the first order terms computed in the case of ^{56}Ni as a function of β_2. The blue line corresponds to the precision of the term derived in [1]. The orange line corresponds to the precision of $f_{N,T,2}$. Both are compared to $f_{2,ex}$.

One can see on figure 3.3 that the error for the Taylor expansion over β_2 is lower than the one for the expression from [1] for $\beta_2 < 0.2$. This trend is inverted for prolate deformations greater than 0.2. One can see in figure 3.4 that the RMS error for both approach goes to zero for $\beta_2 = 0$. All expressions are then exactly equal in the spherical case. Apart from the spherical case, the error increases with the deformation. A very similar behavior can be seen in figure 3.4 : for oblate deformations, the error for the proposed expansion is smaller than the error for the expression provided by [1]. For the range of prolate deformations greater than 0.2, the Kumar-Sørensen formula is more precise than the

proposed expansion. We can see this behavior in figure 3.3. Therefore this trend that appears in the comparison of the first order terms propagates in the comparison of the whole potential.

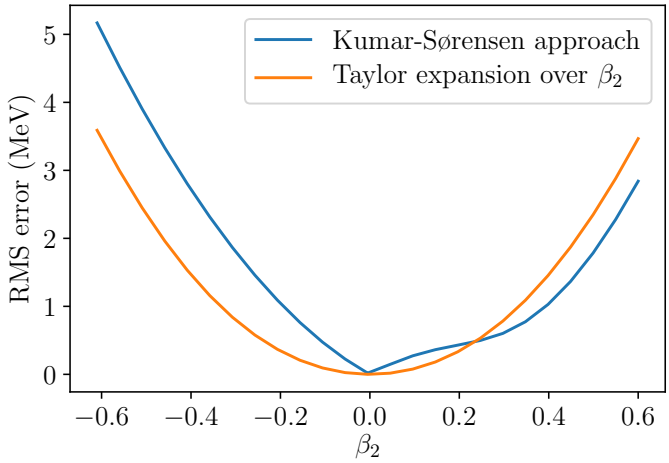

Figure 3.4: RMS error of the total Woods-Saxon potential computed in the case of ^{56}Ni as a function of β_2. The blue line corresponds to the precision of the expression used in [1]. The orange line corresponds to the precision of $V_{N,T}$. Both are compared to V_{proj}.

Figure 3.3 and figure 3.4 show different aspects of both the Kumar-Sørensen correction and the proposed Taylor expansion. Figure 3.3 exposes the error for the first order terms only. We can remark that the curves cross in one point. This shows that the expressions behave differently for prolate and oblate shapes. The error on the Taylor expansion on deformation is smaller than the error on the Kumar-Sørensen formula on a wider range of value (for $-0.6 \leq \beta_2 \leq 0.2$). This is a strong argument to conclude that the proposed expansion is a more precise estimate than the one proposed by Kumar and Sørensen. This trend is confirmed by figure 3.5.

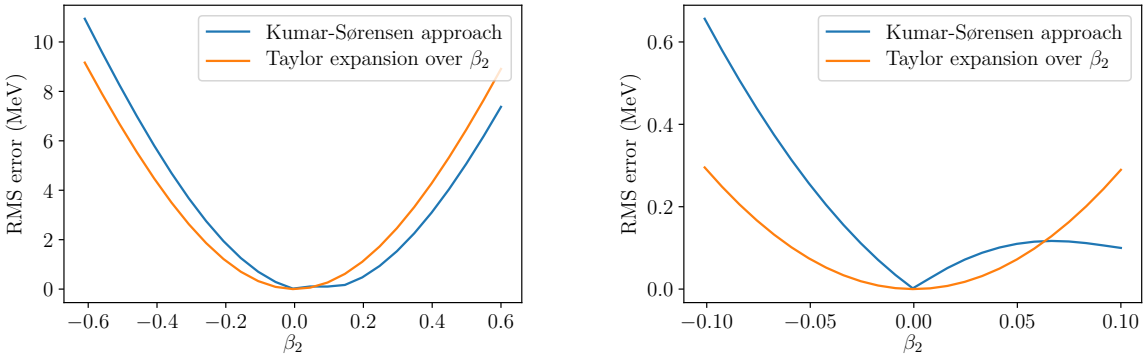

(a) For $-0.6 \leq \beta_2 \leq 0.6$

(b) Close-up around $\beta_2 = 0$.

Figure 3.5: RMS error of the total Woods-Saxon potential computed in the case of ^{56}Ni as a function of β_2. The blue line corresponds to the precision of the expression used in [1]. The orange line corresponds to the precision of $V_{N,T}$. Both are compared to V_{exact}.

The behavior of both errors with respect to V_{exact} is very similar to the ones with respect to V_{proj}. The difference here is that the crossing occurs for a smaller prolate deformation, $\beta_2 = 0.067$. The proposed expansion has still a smaller error on a larger range of values than the Kumar-Sørensen formula, supporting the proposed expansion as a better estimate. One can also note from figure 3.5b that the error on $V_{N,T}$ is smoother than the one on $V_{N,KS}$, and can then be handled more easily in later computations.

To obtain the previous figures, it was necessary to set some parameters, namely the angle θ and the charge and mass number Z and A. The angle θ is in the spherical harmonics which is multiplied to the radial part of the expression. This choice of numerical value can be justified by the fact that the potentials is at its most deformed for $\theta = 0$. This can be seen in figure C.7 in appendix C. As far as charge and mass number are concerned, they only have a minor influence on the proposed results as only A is used in the different formulas to compute the radius R_0.

Visualization of the expansion

To visualize even more directly how the Taylor expansion over the deformation works compared to the exact deformed potential, one can look at a contour representation of the potentials for several values of β_2. This is represented in figure 3.6 (see next page).

The left column shows the contour plots for the exact deformed potential, namely using the equation,

$$V_{exact}(\mathbf{r}) = \frac{W_\tau}{1 + \exp\left(\frac{r - R_0(1+\beta_2 Y_{20}(\theta))}{a}\right)}.$$

The right column shows the contour plots for the potential $V_{N,T}$ from equation (2.8). We can first remark that the exact potential deforms faster than the approximated one. As a consequence, both potentials are very similar close to the spherical shape ($\beta_2 < 0.2$) and look very different as the deformations increase. This is consistent with the fact that the RMS error in figure 3.4 increases with β_2.

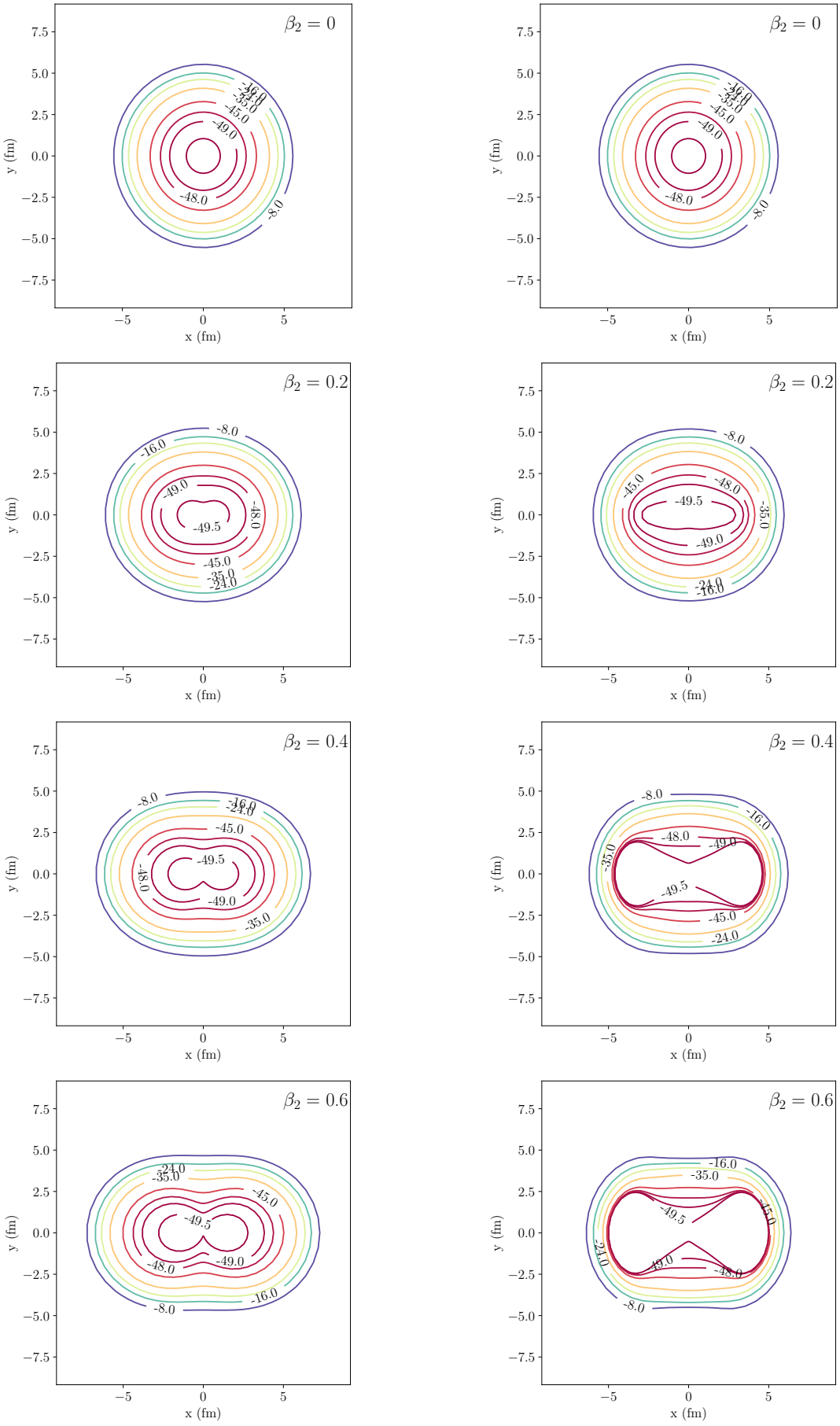

Figure 3.6: Contour plots of the Woods-Saxon potential for ^{56}Ni. *Left column* : exact deformed Woods-Saxon potential. *Right column* : Taylor expansion over the deformation.

We can also see the difference between prolate and oblate values for the deformation parameter. The same contour plots are provided for an oblate deformation in figure 3.7 :

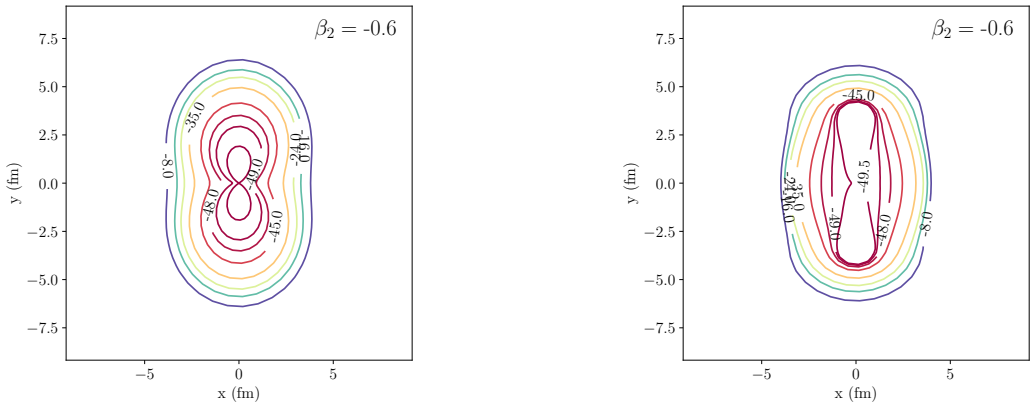

Figure 3.7: Contour plots of the Woods-Saxon potential for oblate deformations for ^{56}Ni. *Left column* : exact deformed Woods-Saxon potential. *Right column* : Taylor expansion over the deformation.

Eventually, to have a complete and direct illustration of the potentials, the 3D equivalents of the contour plots in figure 3.6 are shown in appendix C.

3.1.2 The Coulomb term

To compare the Coulomb term, the same method as for the Woods-Saxon term has been used. The formulas for the RMS error presented in the beginning of chapter 3 have been adapted to the Coulomb potential. The same logic is followed to analyze the performace of the considered approximations.

In figure 3.8, we can first see the total Coulomb potential as a function of the radius for $\theta = 0$ and $\beta_2 = 0.2$.

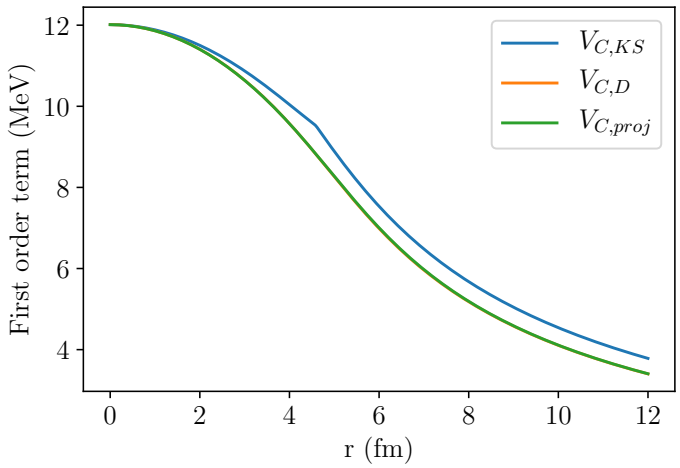

Figure 3.8: Coulomb potential as a function of the radius computed in the case of ^{56}Ni. The blue line corresponds to the potential as computed in [1], the orange line corresponds to equation (2.33), and the green one to the projected potential, for the particular value $\beta_2 = 0.2$ and $\theta = 0$.

One can see in figure 3.9 the quadrupole terms of each expression, providing a clearer view of each estimate's differences :

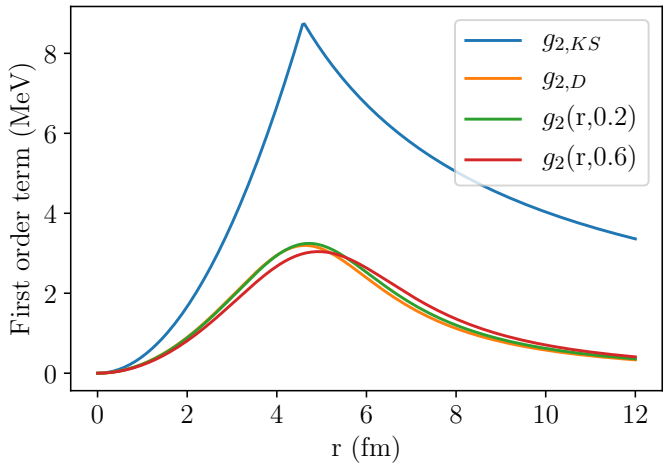

Figure 3.9: First order terms for the Coulomb potential as a function of radius computed in the case of ^{56}Ni. The blue line corresponds to the first order term from [1], the orange line corresponds to the quadrupole term of the proposed decomposition over the density, the green one to the quadrupole term of the projection over the exact density for $\beta_2 = 0.2$, and the red one to the quadrupole term of the projection over the exact density for $\beta_2 = 0.6$.

The green and the orange curves overlap, which makes it almost impossible to distinguish one from the other. In a similar fashion as figure 3.2, the curve for both approximations remains the same as they do not depend on the deformation parameter, and as it grows, the bell for g_2 broadens and becomes more and more different from $g_{2,D}$, and closer to $g_{2,KS}$. This is confirmed by the shape of the RMS errors exposed in figure 3.10 and 3.11.

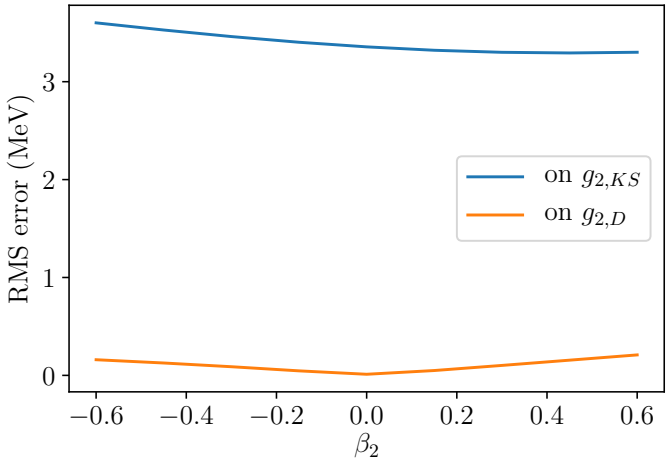

Figure 3.10: RMS error of the quadrupole terms computed in the case of ^{56}Ni as a function of β_2. The blue line corresponds to the precision of the term derived in [1]. The orange line corresponds to the precision of $g_{2,D}$.

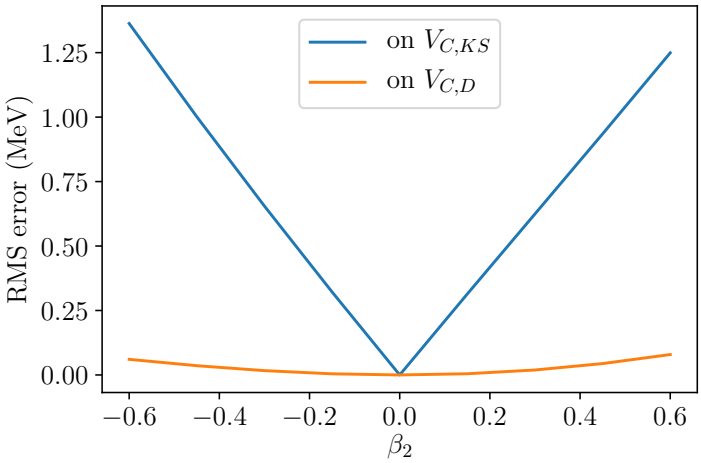

Figure 3.11: RMS error of the total Coulomb potential computed in the case of ^{56}Ni as a function of β_2. The blue line corresponds to the precision of the expression used in [1]. The orange line corresponds to the precision of $V_{C,D}$.

The interpretation of those results is very similar to the one proposed for the Woods-Saxon term, as the method used in both cases is the same. In the same way as for the Woods-Saxon potential, one can first remark that, in figure 3.11, both RMS error for the total potential go to zero for $\beta_2 = 0$. As stated previously, this assures that all proposed models represent exactly the spherical case. The evolution of the error for the Kumar-Sørensen formula and the expansion over the density are very similar as they both increase with the deformations.

As noted previously, figure 3.10 and figure 3.11 shows different features of the proposed expansion over the density and of the estimate of the Coulomb potential proposed in [1]. The error on the quadrupole terms shown in figure 3.10 increases as β_2 increases for the expansion over the density and decreases for the Kumar-Sørensen formula. This is due to the fact that $g_{2,KS}$ and $g_{2,D}$ are β_2-independent, as shown previously. The quadrupole term of the exact potential g_2 then changes with β_2 as the other quadrupole terms remain the same. As β_2 goes from oblate to prolate, the curve for g_2 goes from the negative values to the positive ones, getting closer and closer to $g_{2,KS}$. This explains why the error on $g_{2,KS}$ is strictly decreasing. For the expansion on the density, g_2 gets closer and closer to $g_{2,D}$ as it goes closer to a spherical shape, explaining the minimum for the error for small deformations.

We can see in both figure 3.10 and 3.11 that the curve corresponding to the Kumar-Sørensen formula is always above the one corresponding to the expansion over density. Therefore, one can conclude that the Taylor expansion over the deformation on the density is a better estimate for the Coulomb interaction than the one proposed in [1].

One can finally remark that, as it was the case in the section 3.1.1, choosing a numerical value for the angle θ and picking a particular nucleus (so numerical values for A and Z) was necessary. One can apply the same arguments as in section 3.1.1 for the choice of θ. $^{56}_{28}\mathrm{Ni}_{28}$ is a special nucleus in the sense that 28 is a magic number, making ^{56}Ni doubly magic. This nucleus appears to be stable for a spherical shape [21]. One can try to see whether a heavier nucleus which would be stable for a deformed shape would still behave in the same way as ^{56}Ni. We then perform the same computations on $^{166}_{66}\mathrm{Dy}_{100}$, which is

a heavier nucleus stable for a prolate shape ($\beta = 0.35$) [21]. We keep the same diffuseness as for ^{56}Ni and change R_0 according to equation (3.1), which yields $R_0 \simeq 6.59$ fm. We also keep $\eta = 300$ bur the radius now goes from 0 fm to 15 fm.

Figure 3.12 shows the RMS error for the potentials computed with ^{166}Dy.

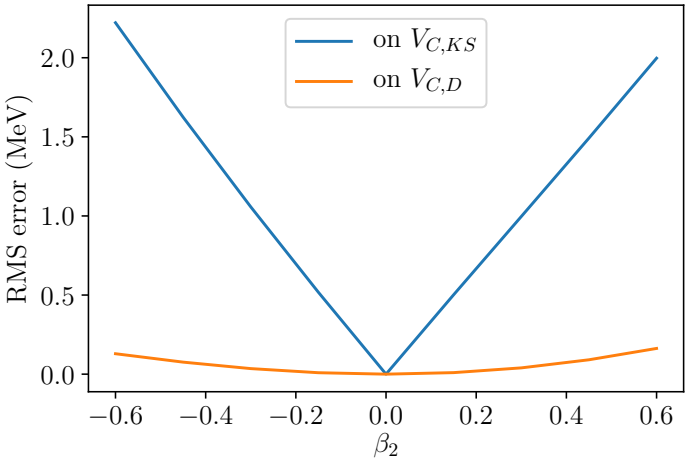

Figure 3.12: RMS error of the total Coulomb potential computed in the case of ^{166}Dy as a function of β_2. The blue line corresponds to the precision of the expression used in [1]. The orange line corresponds to the precision of $V_{C,D}$.

Figure 3.12 and figure 3.11 present a very similar shape for both errors, the only difference being the magnitude. This is an encouraging sign that the proposed approximations would behave in the same way over the whole nuclear landscape. Further investigations are necessary to prove this statement, performing those computations with more nuclei for instance.

3.2 Comparing spectra

The different formulas introduced in sections 2.1 and 2.2 have been compared using the RMS error. We now compare them using the spectra they yield. As explained in section 2.4, we compute the matrix element of the Hamiltonian built with these expression and diagonalize the resulting matrix,

$$\begin{aligned} H_{HOSPHE} &= T + V_N + V_{C,KS} + V_{SOKS} \\ &= T + V_\tau^{sph}(r) + \beta_2 Y_{20}(0)(-f_{N,2}(r) + g_{2,KS}(r) + f_{2,SOKS}(r)). \end{aligned} \tag{3.6}$$

We eventually plot the eigenvalues as a function of the deformation parameter β_2. For the numerical values of the different parameters, we use the so called *universal* parameterization from [19].

This process shows the impact of each term on the total Hamiltonian. We implement the derived approximations and generate the corresponding spectra in HOSPHE, and compare them with the complete one provided by WSBETA. On the one hand, WSBETA, as described in section 2.4, gives the spectrum of considered nucleus under a deformed Woods-Saxon

using the formulas that we consider exact. On the other hand, HOSPHE's structure enables to implement the desired operators, under the condition that they have the required form, as mentioned in section 2.4. Therefore, using these two programs, we can compare the approximations to their corresponding exact versions.

We have implemented in HOSPHE the Kumar-Sørensen formula and the proposed expansion for the Woods-Saxon term (equations (2.7) and (2.8)).However, the proposed expansion over the density for the Coulomb potential (equation (2.33)) contains several integrals. *Fortran* does not provide a ready-made routine for integration, and the better options and algorithms to do so have not been investigated. *Python* does (subpackage *scipy.integrate*) which gives us the possibility to compare the approximations that contains integrals. We therefore kept the Kumar-Sørensen formula for the Coulomb term for the implementation in *Fortran*.

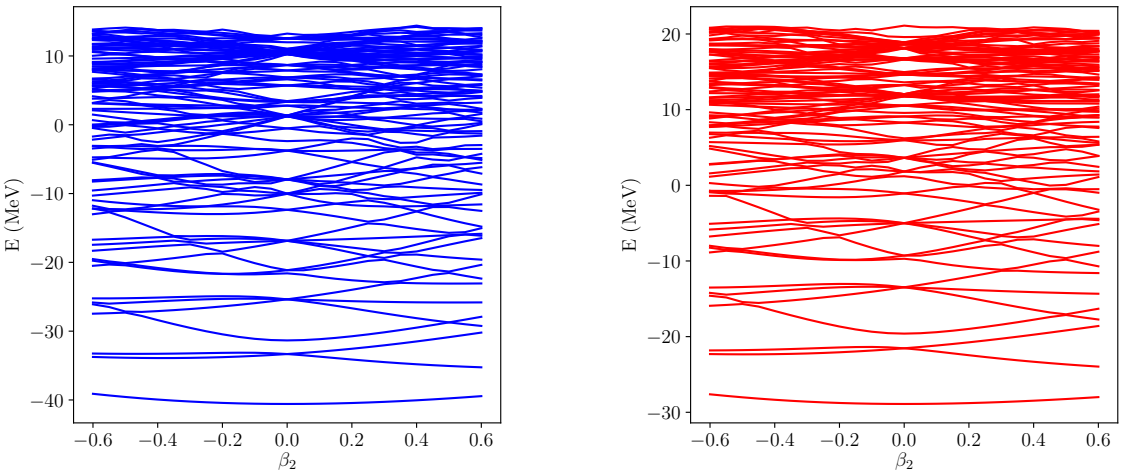

(a) for neutrons (b) for protons

Figure 3.13: Spectra for ^{56}Ni under a deformed Woods-Saxon potential calculated with WSBETA.

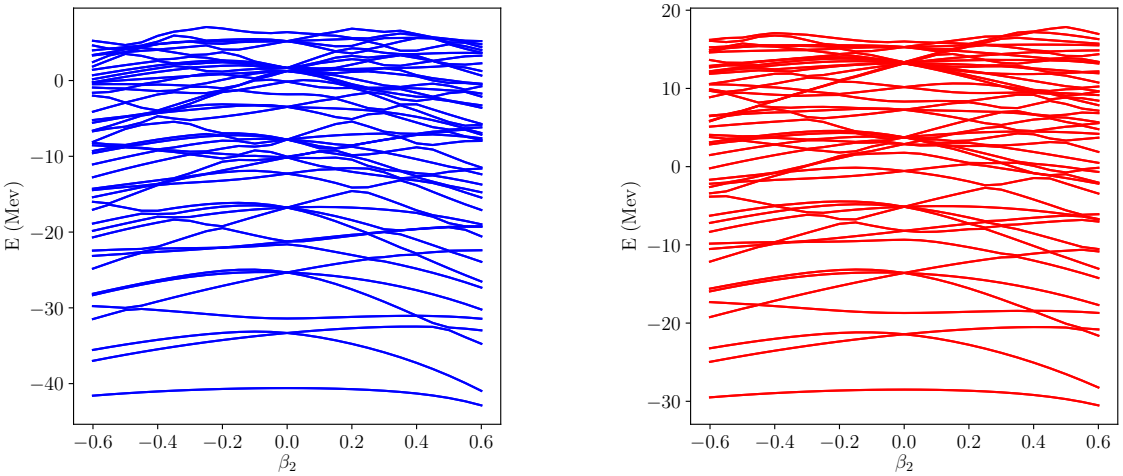

(a) for neutrons (b) for protons

Figure 3.14: Spectra for ^{56}Ni calculated with HOSPHE using $V_{N,T}$.

Both programs provide the 92 first states of the system. The levels are degenerated for

$\beta_2 = 0$ and split when the system is deformed. We can see right away, thanks to this feature if the computed spectra have the appropriate aspect.

We notice here that the levels in the spectra provided by HOSPHE are bent in the other direction, comparatively to the spectra computed with WSBETA. This feature seems to be consistent for the whole spectrum. This difference can be due to a different treatment of volume conservation in both cases and to the differences in implementation of the deformations in both codes. To cancel this effect and have more direct comparisons, we can substract the first level to all the other levels. This way, all the levels will be straightened, and the first level will be completely flat, and all the energies will be shifted so that the first level is at exactly 0 MeV. This is shown in figures 3.15 and 3.16.

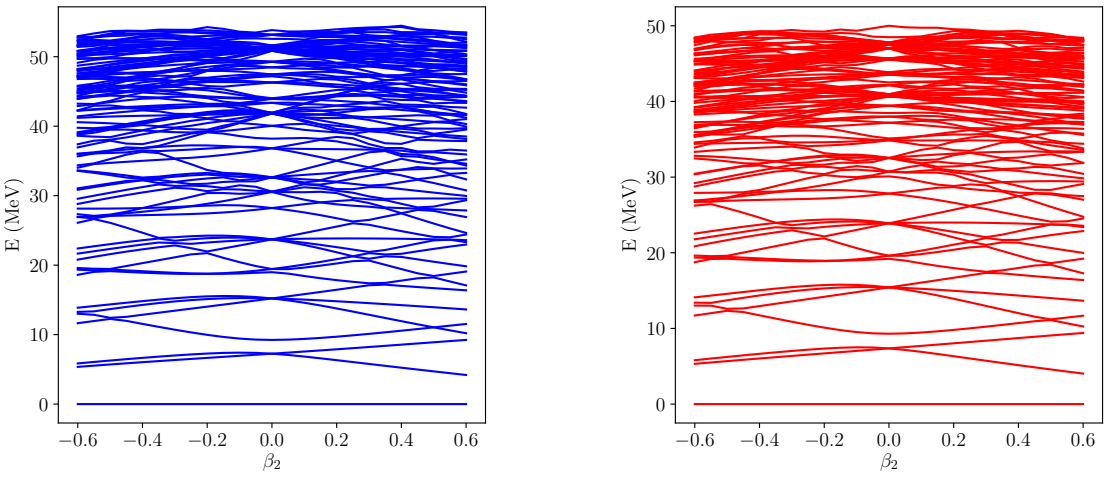

(a) for neutrons (b) for protons

Figure 3.15: Spectra for ^{56}Ni under a deformed Woods-Saxon potential calculated with WSBETA, correcting with the first level.

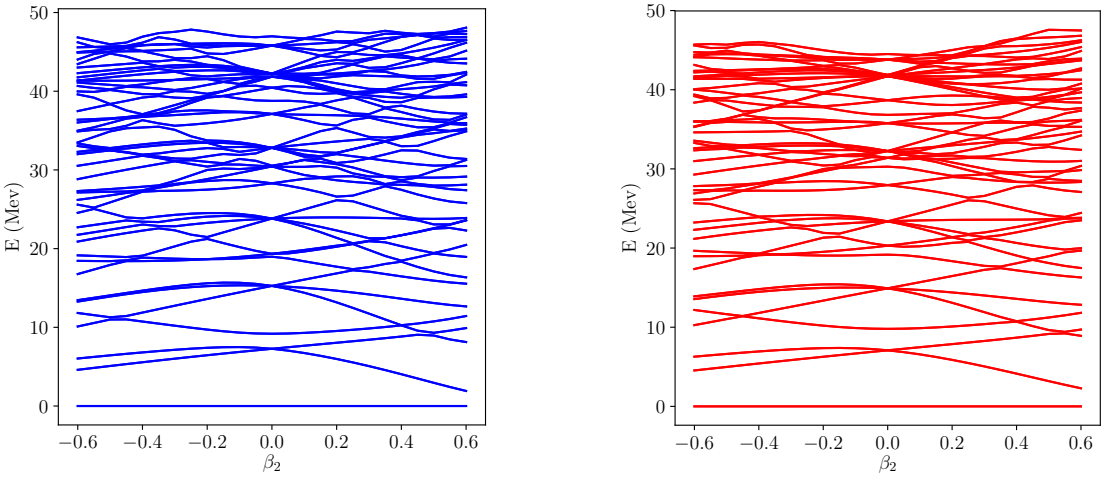

(a) for neutrons (b) for protons

Figure 3.16: Spectra for ^{56}Ni calculated with HOSPHE using the proposed expressions, substracting the first level, computed using $V_{N,T}$.

Figure 3.15 and 3.16 present the same features. The crossing of every level for $\beta_2 = 0$

is visible and the bound states (those under 40.6 MeV, which is the absolute energy of the most bound particle) have the same energies. The levels split when the nucleus is deformed. As a consequence, levels cross each other again for certain values of $\beta_2 \neq 0$. We can then compare the different expressions analyzing the intersections of the levels for deformed shapes. The spectra for neutrons for ^{56}Ni computed using $V_{N,T}$ and $V_{N,KS}$ are shown in figure 3.17.

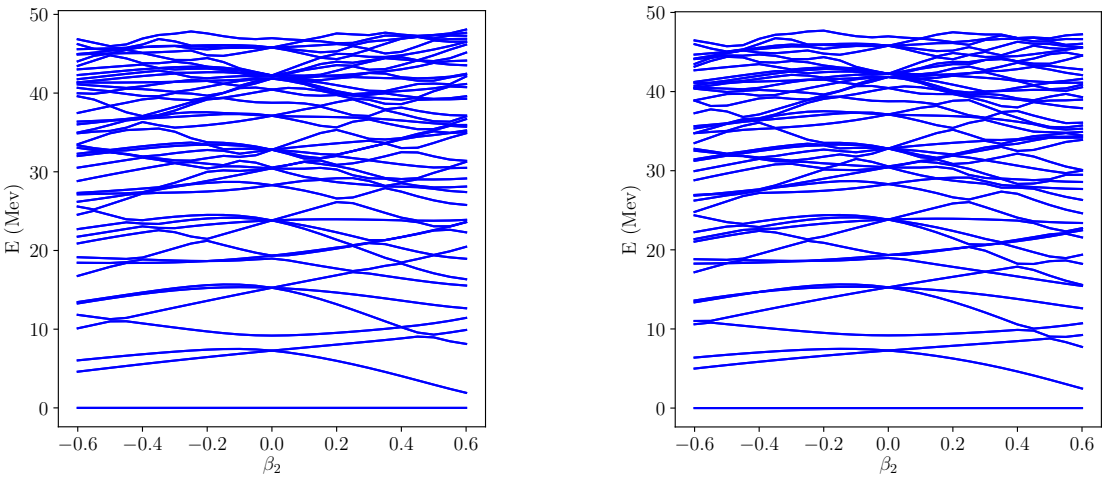

(a) using $V_{N,T}$ (b) using $V_{N,KS}$

Figure 3.17: Spectra for ^{56}Ni for neutrons calculated with HOSPHE using $V_{N,T}$ or $V_{N,KS}$.

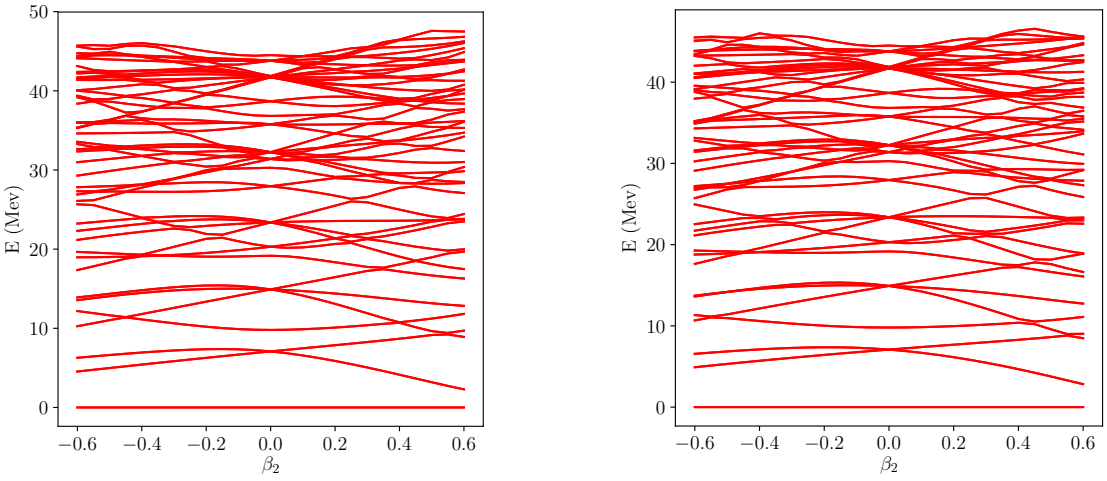

(a) using $V_{N,T}$ (b) using $V_{N,KS}$

Figure 3.18: Spectra for ^{56}Ni for protons calculated with HOSPHE using $V_{N,T}$ or $V_{N,KS}$.The Coulomb term is $V_{C,KS}$.

We can see in figure 3.17a that for oblate deformations, the levels cross each other for a lower β_2. We can take the example of the crossing at $\beta_2 = -0.5$, E = 12 MeV. In figure 3.17b, this intersection can be seen at another point in the spectra, for $\beta_2 = -0.6$, E = 12 MeV. Figure 3.17a shows then more agreement with figure 3.15a, where the same crossing happens for $\beta_2 = -0.5$ as well, than figure 3.17b. This similarity can be observed for more crossings for high oblate deformations ($\beta_2 < -0.4$). This is another

evidence that the proposed expansion $V_{N,T}$ for the Woods-Saxon term is closer to the exact potential than the one proposed by Kumar and Sørensen in [1], $V_{N,KS}$. We perform the same comparison for protons, where the Coulomb interaction acts on the system. This is shown in figure 3.18. For both spectra, the Coulomb term is given by $V_{C,KS}$.

We can here give the same interpretation as the one proposed for figure 3.17. A crossing also appears at the same location as for neutrons for $\beta_2 = -0.5$, E = 10 MeV in figure 3.18b. This intersection occurs for $\beta_2 = -0.6$, E = 10 MeV, in figure 3.18a. Figure 3.15b displays it for $\beta_2 = -0.5$, which constitues an additional argument in favor of the Taylor expansion over β_2.

This particular intersection of the levels, both for neutrons and protons, is just an example to show the type of observations that can be done on the spectra to compare the different expressions. There exist several other crossings of the same type at other locations on the spectra where the same analysis is possible. For example, the intersection for $\beta_2 = -0.4$, E = 18 MeV, in figure 3.15b is visible at the same location in figure 3.17a, but is shifted towards higher β_2 in figure 3.17b, supporting $V_{N,T}$ as a more precise approximation.

We have now considered the spectra in the particular case of a double magic nucleus, ^{56}Ni. We can also consider a heavier nucleus, stable for a deformed shape. A nucleus with these features is ^{166}Dy. Figure 3.19 shows the spectra computed with WSBETA and figure 3.20 shows the spectra computed with HOSPHE (see next page).

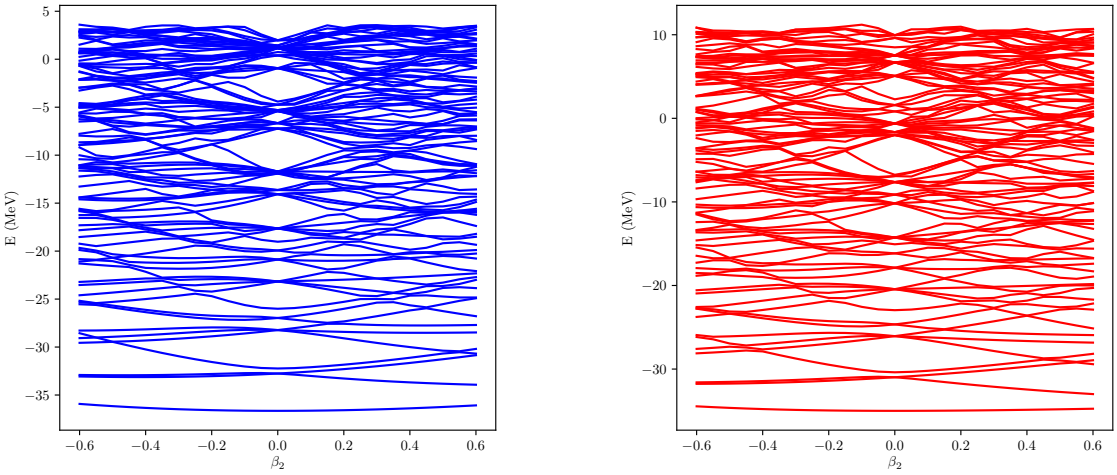

(a) for neutrons (b) for protons

Figure 3.19: Spectra for ^{166}Dy under a deformed Woods-Saxon potential computed with WS-BETA.

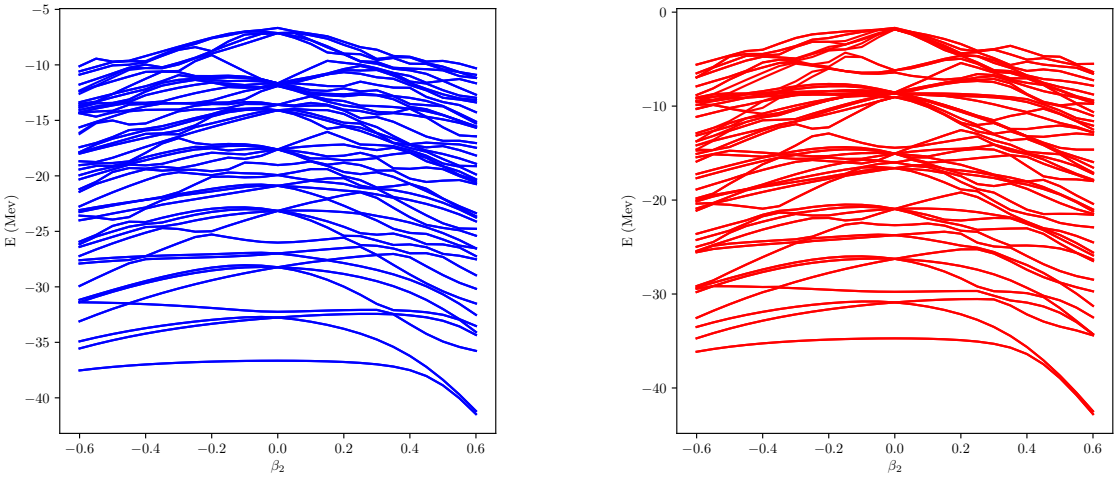

(a) for neutrons (b) for protons

Figure 3.20: Spectra for ^{166}Dy calculated with HOSPHE using $V_{N,T}$ for the Woods-Saxon term.

Qualitatively, we can see that the behavior of the states around the spherical shape in figure 3.20 is rather similar to the one in figure 3.19 and to the one that can be observed on the spectra for ^{56}Ni. But for larger prolate deformations ($\beta_2 > 0.4$), all the levels tend to be shifted towards lower energies on the spectrum yielded by HOSPHE. This can be explained by the fact that, for a larger A, the Woods-Saxon potential computed using the Kumar-Sørensen approximation is less smooth than for ^{56}Ni. This can be seen in figure C.5 in appendix C. The potential shows two sharp wells for high prolate deformations. The first levels would then be at the bottom of the potential wells, explaining this displacement. This might be a sign that, for more exotic or heavier nuclei, the range of validity of the model is smaller than the one of lighter nuclei. For larger nuclei, the wells become too sharp for large deformations and the expansion does not estimate the exact potential in a satisfactory way. On the one hand, one could imagine solving this issue considering higher order terms, in β_2^2 or even in β_2^3, in the Taylor expansion. On the other hand, one could

consider more multipole deformations to make the projected potential smoother even for heavy nuclei. This latter option looks more efficient according to figure C.4 in appendix C. This figure displays the Woods-Saxon potential computed using the projected expression V_{proj}. The first order term of V_{proj} includes the deformations directly in the exponential, and therefore includes all the orders of β_2. The potential in figure C.4 also shows those two sharp wells, which would support the idea that adding more multipole deformations will help smoothen the potential. Adding Y_{40} and Y_{60} terms is direct if one follows the same process as in this thesis. Testing the resulting expressions on a greater number of nuclei constitutes an interesting sequel to this thesis.

Chapter 4

Conclusion and outlook

The aim of this work was to investigate a new expression for an effective Hamiltonian that could then be mapped to DFT. The starting point of this operator is the Pairing-Plus-Quadrupole model and a formula for the quadrupole part proposed by Kumar and Sørensen in [1]. The idea is then to propose an alternative to each term of the Kumar-Sørensen formula, which are the Woods-Saxon term, the Coulomb term and the spin-orbit term. Those new formulas would provide a more precise description of the physical phenomena and would include the physics related to nuclear deformations. Those new expressions and the one from [1] remain approximations. So to determine what approximation is the most accurate, we compare the proposed expression and the Kumar-Sørensen expression for it to a projection of the exact formula for each interaction. This comparison has been carried out first using the RMS error, depending on the deformation, between each expression and the projection of the exact potentials. To compare the effect of different terms in the full expression, we plotted the spectra with and without the Coulomb interaction and compared the behavior of the energy levels with deformation to exact results.

After this process and the obtained results, we are inclined to think that the Taylor expansion over the deformation parameter is a good estimate of the deformed Woods-Saxon term, and that the Taylor expansion over the deformation for the proton density yields a good estimate for the Coulomb term. This leads to the following modified quadrupole potential,

$$V_Q(r,\theta) = \frac{1}{2}(1-\tau)H_C(r) + W_\tau(f(r) - \frac{1}{2}v_{so}\lambda^2(\mathbf{p}\times\mathbf{s})\cdot\nabla f(r)) \\ + Y_{20}(\theta)\beta_2\left(-R_0W_\tau\left.\frac{\partial V_T(\mathbf{r})}{\partial\beta_2}\right|_{\beta_2=0} + \frac{1}{2}(1-\tau)g_{2,D}(r) + \frac{1}{2}W_\tau v_{so}\lambda^2\frac{\partial^2 f(r)}{\partial r^2}\mathbf{l}\cdot\mathbf{s}\right),$$

with,

$$
\begin{aligned}
f(r) &= \frac{1}{1+\exp(\frac{r-R_0}{a})}, \\
V_T(\mathbf{r}) &= \frac{W_\tau}{1+\exp(\frac{r-R_0(1+\beta_2 Y_{20}(\theta))}{a})} \\
H_C(r) &= \frac{Ze^2}{4\pi\epsilon_0}\left(\frac{1}{r}\Theta(r-R_c)+\frac{1}{R_c}\left(\frac{3}{2}-\frac{1}{2}\left(\frac{r}{R_c}\right)^2\right)\Theta(R_c-r)\right), \\
g_{2,D}(r) &= \frac{e^2}{4\pi\epsilon_0}\frac{4\pi}{5}\left(\frac{1}{r^3}\int_0^r q^4\rho^{(2)}(q)dq + r^2\int_r^\infty \frac{1}{q}\rho^{(2)}(q)dq\right), \\
Y_{20}(\theta) &= \frac{1}{4}\sqrt{\frac{5}{\pi}}(3\cos^2(\theta)-1).
\end{aligned}
$$

Kumar and Sørensen propose an expression that has a spherical part completed with a radial correction multiplied by the deformation parameter and the Y_{20} spherical harmonics. This feature is preserved in V_Q, which makes it suitable to be implemented in HOSPHE. We can now extract the form factor from V_Q in the same way as in [1]. It yields the following result,

$$
P(r) = R_0 W_\tau \left.\frac{\partial V_T(\mathbf{r})}{\partial \beta_2}\right|_{\beta_2=0} + \frac{1}{2}(1-\tau)g_{2,D}(r) + \frac{1}{2}W_\tau v_{so}\lambda^2\frac{\partial^2 f(r)}{\partial r^2}\mathbf{l}\cdot\mathbf{s}
$$

To have an even more complete study, one could try to implement the expansion over the density for the Coulomb term. This can be done using a numerical method or quadrature, or by tabulating the values of the integrals for several nuclei. To push the computations further, one could try to perform the same computations varying the angle θ. This way, it would be possible to investigate the behavior of the error on the different approximations on a 2D space, giving a more complete view of the different expressions. As explained in section 3.2, adding other multipole terms and testing the expressions on more nuclei would help extending the range of validity of the proposed expressions. Finding a more efficient formula for the spin-orbit interaction by finding a physical situation to test the model would eventually complete the modified quadrupole force. The final step to have a complete approach to the Pairing-Plus-Quadrupole Hamiltonian is to add the pairing potential and, if possible, refine it as well.

Bibliography

[1] K. Kumar, B. Sørensen, *Derivation of the Radial Dependence of the Quadrupole Force from a Woods-Saxon Potential*, Nucl. Phys. **A146** (1970) 1

[2] K. Capelle, *A Bird's-Eye View of Density-Functional Theory*, Braz. J. Phys. 36 **4A** (2006) 1318

[3] P. Hohenberg, W. Kohn, *Inhomogeneous Electron Gas*, Phys. Rev. **136** (1964) B864

[4] W. Kohn, L.J. Sham, *Self-Consistent Including Exchange and Correlation Effects*, Phys. Rev. **140** (1965) A1133

[5] T. H. R. Skyrme, *The Effective Nuclear Potential*, Nucl. Phys. **9** (1959) 615

[6] A. Bohr, B.R. Mottelson, *Beta-Decay and the Shell Model, and the Influence of Collective motion on Nuclear Transitions*, Physica XVIII **12** (1952) 1066

[7] A. Bohr, B.R. Mottelson, *Interpretation of Isomeric Transitions of Electric Quadrupole Type*, Phys. Rev. **89** (1953) 316

[8] A. Bohr, B.R. Mottelson, *Collective and Individual-Particle Aspects of Nuclear Structure*, Mat. Fys. Medd. Dan. Vid. Selsk. **27**, no 16 (1953)(ed 2, 1957)

[9] B. Sørensen, *On the Description of Fermion States in Boson Representations*, Nucl. Phys. **A97** (1967) 1

[10] A. Arima, F. Iachello, *Collective Nuclear States as Representations of a SU(6) Group*, Phys. Rev. Lett. **35** (1975) 1069

[11] M. Moshinsky, *Confrontation of Nuclear Collective Models*, Nucl. Phys. **A338** (1980) 156

[12] L. Kisslinger, R. Sorensen, *Spherical Nuclei with Simple Residual Forces*, Rev. Mod. Phys. **35** (1963) 853

[13] P. Ring, P. Schuck, *The Nuclear Many-Body Problem* (Springer, 1980)

[14] S. G. Nilsson, I. Ragnarsson, *Shapes and Shells in Nuclear Structure* (Cambridge University Press, 1995)

[15] M. Baranger, K. Kumar, *Nuclear Deformations in the Pairing-Plus-Quadrupole Model, (I). The Single-j Shell*, Nucl. Phys. **62** (1965) 113

[16] R.W. Hasse, W.D. Myers, *Geometrical Relationships of Macroscopic Nuclear Physics* (Springer, 1988)

[17] D.A. Varshalovich, A.N. Moskalev, V.K. Khersonskii, *Quantum Theory of Angular Momentum* (World Scientific, 1988)

[18] V.A. Chepurnov, P.E. Nemirovsky, *Spin-Orbit Interaction in Deformed Nuclei*, Nucl. Phys. **49** (1963) 90

[19] S. Cwiok, J. Dudek, W. Nazarewicz, J. Skalski, T. Werner, *Single-Particle Energies, Wave Functions, Quadrupole Moments and g-Factors in an Axially Deformed Woods-Saxon Potential with Applications to the Two-Centre-Type Nuclear Problems*, Comput. Phys. Commun. **46** (1987) 379

[20] B.G. Carlsson, J. Dobaczewski, J. Toivanen, P. Veselý, *Solution of self-consistent equations for the N^3LO nuclear energy density functional in spherical symmetry. The program* HOSPHE *(v1.02)*, Comput. Phys. Commun. **181** (2010) 1641

[21] S. Hilaire, M. Girod, *The AMEDEE Nuclear Structure Database*, AIP Conference Proceedings **1012** (2008) 359

Appendices

Appendix A

The Kohn-Sham algorithm

The Hohenberg-Kohn theorem sets the fundamental principle of DFT. The next step is then to find a convenient and flexible way to apply this result to actual physical problems. This was made possible by the Kohn-Sham equations and algorithm, developed by Walter Kohn and Lu Jeu Sham in 1965 [4].

The Kohn-Sham equations can be derived from the equations written in the previous paragraph. The following calculations are made in the case of an electron gas. We can first write,

$$T[n] = T_s[n] + T_c[n], \tag{A.1}$$

$$U[n] \simeq U_H[n]. \tag{A.2}$$

All quantities are functionals of the electronic density n. One can note that the kinetic energy operator used previously in chapters 2 and 3 corresponds to T_s. The definition of T in this appendix differs from the one used in the rest of the thesis. The kinetic energy of the system T can be separated in two parts : one representing non-interacting particles (with the index s for *single-particles*), and one representing the rest (with the index c for *correlation*). U_H is here the interaction energy computed under the Hartree approximation (see [2] for more details about the exact shape of those functionals). We then write the total energy of the system,

$$\begin{aligned} E[n] &= T[n] + U[n] + V[n] \\ &= T_s[n] + U_H[n] + E_{xc}[n] + V[n] \\ &= \int v(\mathbf{r}) n(\mathbf{r}) d\mathbf{r} + \frac{1}{2} \iint \frac{n(\mathbf{r}) n(\mathbf{r}')}{\mid \mathbf{r} - \mathbf{r}' \mid} d\mathbf{r} d\mathbf{r}' + E_{xc}[n] + T_s[n]. \end{aligned} \tag{A.3}$$

E_{xc} is called the exchange-correlation energy. It comprises the correlation part of the kinetic energy and the difference $U[n] - U_H[n]$. The single-particle part of the kinetic energy depends on the single-particle orbitals of the system. We can assume the following shape for the exchange-correlation energy,

$$E_{xc}[n] = \int n(\mathbf{r}) \epsilon_{xc}(n(\mathbf{r})) d\mathbf{r}, \tag{A.4}$$

with ϵ_{xc} the exchange-correlation energy for one electron of a uniform electron gas. This quantity is accessible from what is known of uniform electron gas. Then, from equation

(A.3) and equation (A.4), we can write,

$$\varphi(\mathbf{r}) = v(\mathbf{r}) + \int \frac{n(\mathbf{r}')}{\mid \mathbf{r} - \mathbf{r}' \mid} d\mathbf{r}', \tag{A.5}$$

$$\mu_{xc}(n) = \frac{dn\epsilon_{xc}}{dn}, \tag{A.6}$$

$$(-\frac{1}{2}\Delta + [\varphi(\mathbf{r}) + \mu_{xc}(n(\mathbf{r}))])\psi_i(\mathbf{r}) = \epsilon_i\psi_i(\mathbf{r}), \tag{A.7}$$

$$n(\mathbf{r}) = \sum_{i=1}^{n} \mid \psi_i(\mathbf{r}) \mid^2 . \tag{A.8}$$

Those four equations are known as the Kohn-Sham equations. Equation (A.7) is the single-particle Schrödinger equation. This derivation is taken from [4] and further mathematical details and notations can be found there as well.

The great interest of those equations is that they introduce at the same time a self-consistent loop to solve them :

1. Assume a density $n(\mathbf{r})$
2. Construct φ from equation (A.5)
3. Construct μ_{xc} from equation (A.6)
4. Construct $n(\mathbf{r})$ from equations (A.7) and equation (A.8)
5. Repeat steps 2, 3 and 4 until convergence

These steps and equations can be adapted for a big amount of different cases. This loop can be directly programmed on a computer to then provide solutions (exact in some precise cases) to a wide range of physical problems.

Appendix B

The Kumar-Sørensen formula for the spin-orbit interaction

The spin-orbit interaction being state-dependent, it requires some additional efforts to find a simple expression for it. This work has been made by Kumar and Sørensen in [1]. So to understand in a better way the form the expression for the spin-orbit interaction in [1], a derivation is proposed in this appendix.

The main tool to reach the expression proposed by Kumar and Sørensen is a Taylor expansion over r of,

$$V_{SO}(r) = -\frac{1}{2} W_\tau v_{so} \lambda^2 (\mathbf{p} \times \mathbf{s}) \cdot \nabla f(r). \tag{B.1}$$

This yields,

$$\begin{aligned} V_{SOKS}(\mathbf{r}) &= V_{SO}(r) - \beta r \frac{\partial V_{SO}(r) Y_{20}(\theta)}{\partial r} \\ &= V_{SO}(r) + \frac{1}{2} r W_\tau v_{so} \lambda^2 \beta (\mathbf{p} \times \mathbf{s}) \cdot \nabla \left(\frac{\partial f}{\partial r} Y_{20}(\theta) \right). \end{aligned} \tag{B.2}$$

For an operator of the shape $(A \times B) \cdot C$, all circular permutation are equal. We apply this property to $(\mathbf{p} \times \mathbf{s}) \cdot \nabla$ and obtain,

$$V_{SOKS}(\mathbf{r}) = V_{SO}(r) + \frac{1}{2} r W_\tau v_{so} \lambda^2 \beta (\nabla \times \mathbf{p}) \cdot \mathbf{s} \left(\frac{\partial f}{\partial r} Y_{20}(\theta) \right). \tag{B.3}$$

We then develop the ∇ operator,

$$V_{SOKS}(\mathbf{r}) = V_{SO}(r) + \frac{1}{2} r W_\tau v_{so} \lambda^2 \beta \left(Y_{20}(\theta) \frac{\partial^2 f}{\partial r^2} (\mathbf{n_r} \times \mathbf{p}) \cdot \mathbf{s} + \frac{1}{r} \frac{\partial Y_{20}}{\partial \theta} (\mathbf{n}_\theta \times \mathbf{p}) \cdot \mathbf{s} \frac{\partial f}{\partial r} \right). \tag{B.4}$$

We eventually use the following the fact that $\mathbf{p} = \mathbf{l} \times \mathbf{r} = \mathbf{l} \times \mathbf{n_r}$) to have,

$$(\mathbf{n_r} \times \mathbf{p}) \cdot \mathbf{s} = \frac{1}{r} \mathbf{l} \cdot \mathbf{s}, \tag{B.5}$$

yielding consequently,

$$V_{SOKS}(\mathbf{r}) = V_{SO}(r) + W_\tau v_{so} \lambda^2 \beta \left(\frac{1}{2} Y_{20}(\theta) \frac{\partial^2 f}{\partial r^2} \mathbf{l} \cdot \mathbf{s} + \frac{3}{2} \sqrt{\frac{5}{4\pi}} \cos\theta \sin\theta (\mathbf{n}_\theta \times \mathbf{p}) \cdot \mathbf{s} \frac{\partial f}{\partial r} \right). \tag{B.6}$$

Appendix C

3D plots of the Woods-Saxon potential

This appendix exposes the 3D version of the contour plots in figure 3.6. The figures showing the Woods-Saxon potentials for ^{166}Dy have also been added.

We can clearly see the sharper shape of the potential when it is computed using the Taylor expansion over the deformation, while the exact potential is a lot smoother. We can see in figure C.6 and figure C.7 those potentials as projected over r and θ to see more clearly their dependence on those parameters.

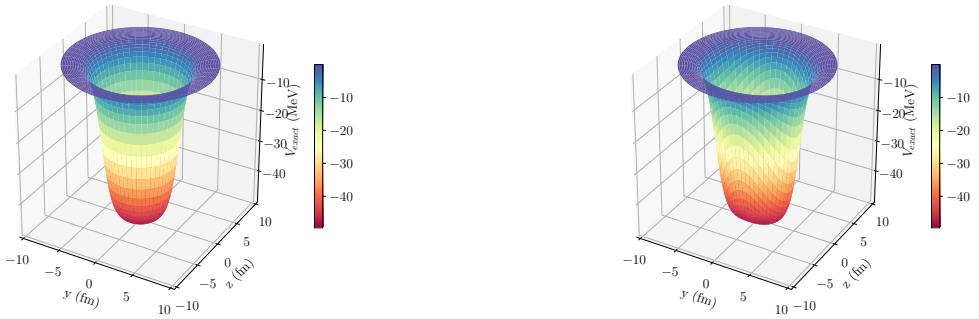

(a) $\beta_2 = 0$ (b) $\beta_2 = 0.2$

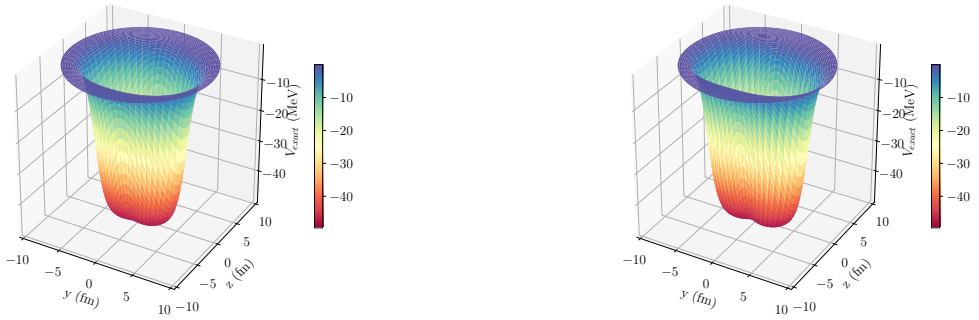

(c) $\beta_2 = 0.4$ (d) $\beta_2 = 0.6$

Figure C.1: The Woods-Saxon potential for ^{56}Ni using the exact deformed potential formula.

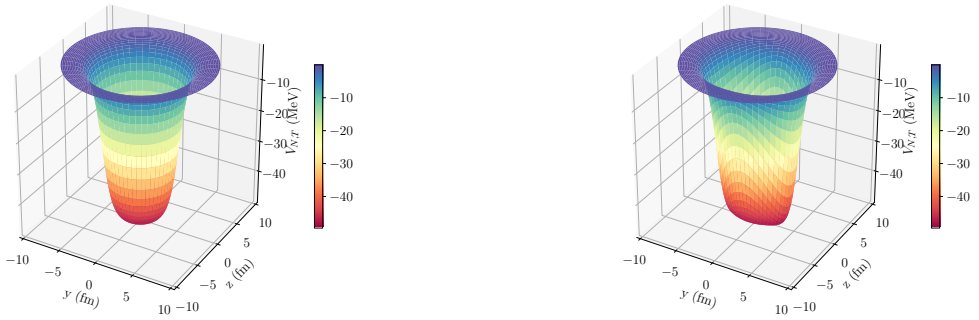

(a) $\beta_2 = 0$ (b) $\beta_2 = 0.2$

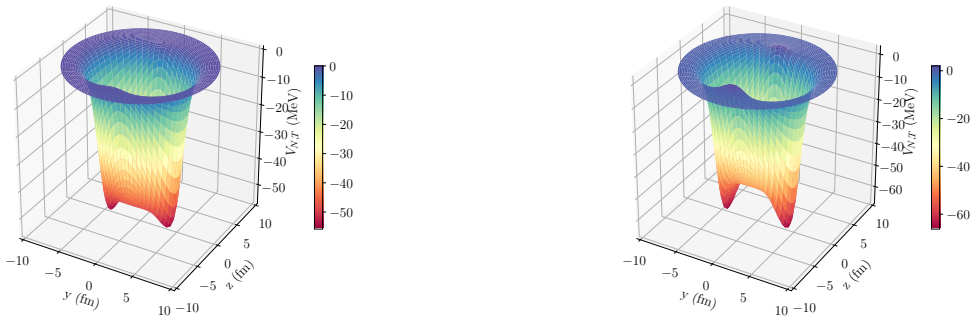

(c) $\beta_2 = 0.4$ (d) $\beta_2 = 0.6$

Figure C.2: The Woods-Saxon potential for ^{56}Ni computed using the Taylor expansion over the deformation.

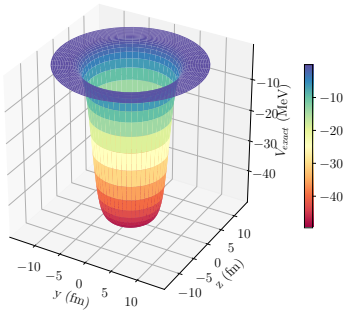

(a) $\beta_2 = 0$

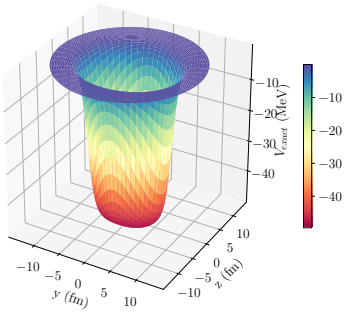

(b) $\beta_2 = 0.2$

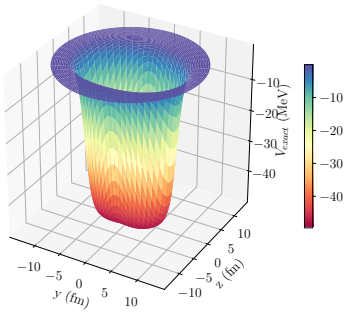

(c) $\beta_2 = 0.4$

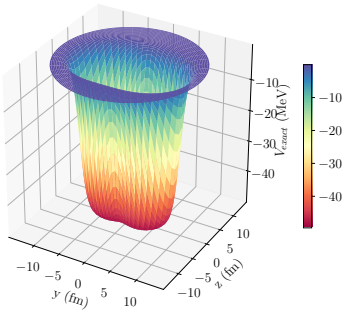

(d) $\beta_2 = 0.6$

Figure C.3: The Woods-Saxon potential for ^{166}Dy using the exact deformed potential formula.

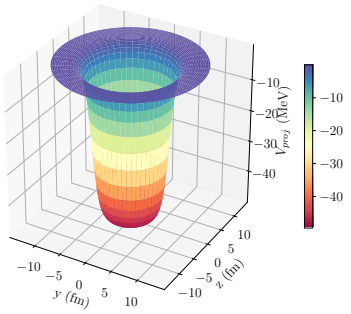

(a) $\beta_2 = 0$

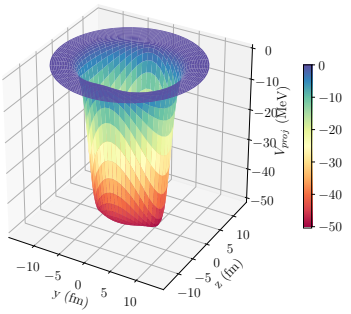

(b) $\beta_2 = 0.2$

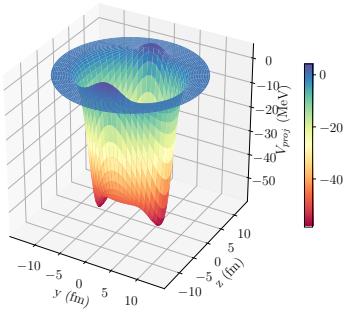

(c) $\beta_2 = 0.4$

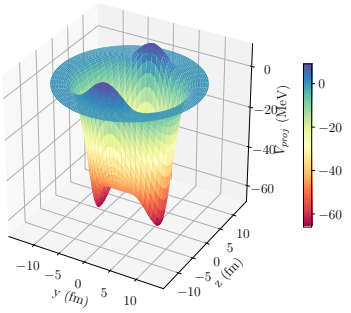

(d) $\beta_2 = 0.6$

Figure C.4: The projected V_{proj} Woods-Saxon potential for ^{166}Dy.

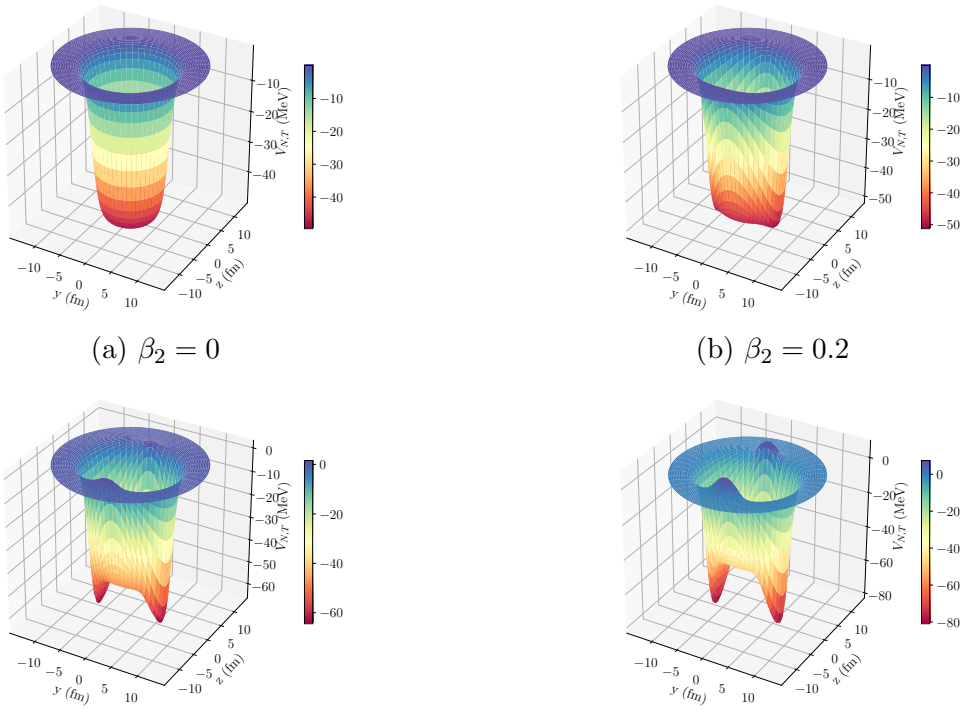

(a) $\beta_2 = 0$ (b) $\beta_2 = 0.2$

(c) $\beta_2 = 0.4$ (d) $\beta_2 = 0.6$

Figure C.5: The Woods-Saxon potential for ^{166}Dy computed using the Taylor expansion over the deformation.

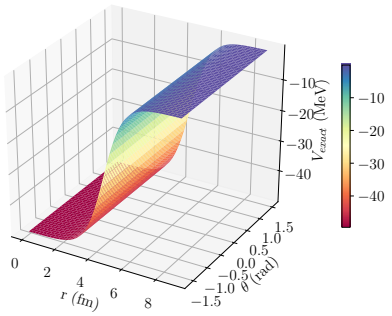

(a) $\beta_2 = 0$

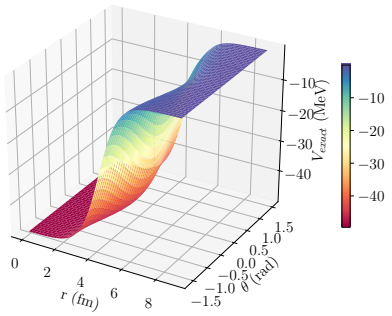

(b) $\beta_2 = 0.2$

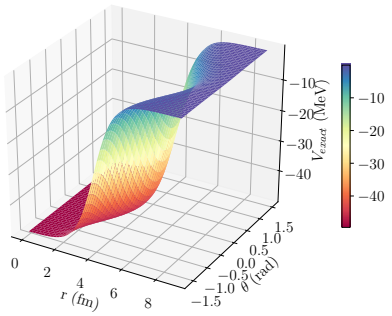

(c) $\beta_2 = 0.4$
chapters

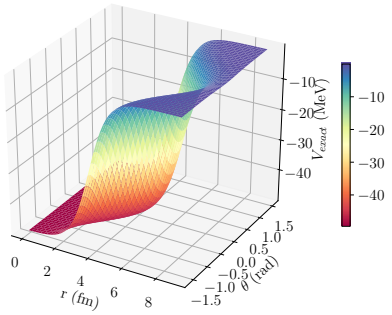

(d) $\beta_2 = 0.6$

Figure C.6: The Woods-Saxon potential for ^{56}Ni using the exact deformed potential formula, projected on the variables r and θ.

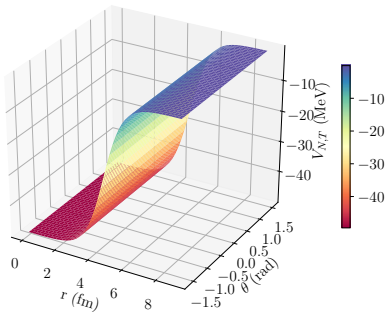

(a) $\beta_2 = 0$

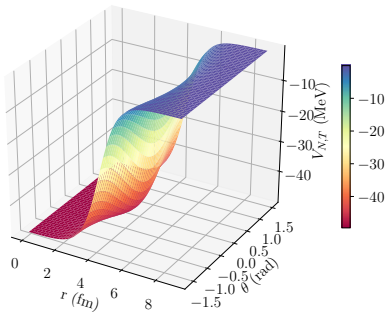

(b) $\beta_2 = 0.2$

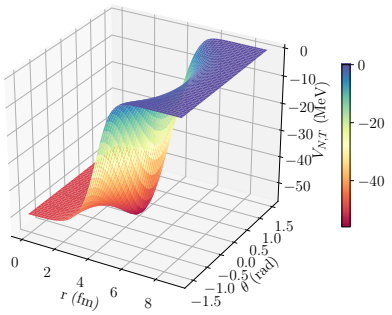

(c) $\beta_2 = 0.4$

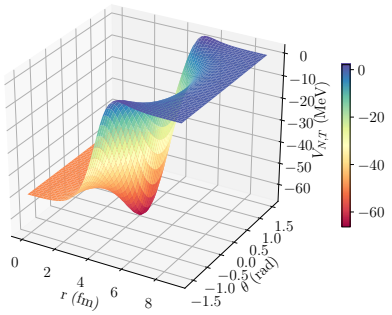

(d) $\beta_2 = 0.6$

Figure C.7: The Woods-Saxon potential for ^{56}Ni computed using the Taylor expansion over the deformation, projected on the variables r and θ.

Popular science summary

A strange bag full of strange marbles

Matter is made of atoms that are constituted by a massive core, called nucleus, with charges, called electrons, orbiting around it. The nucleus itself is made up of two types of particles : protons and neutrons. Neutrons are not electrically charged, unlike protons which are positively charged. The atomic nucleus can be imagined like a bag full of marbles, some neutrals, some are charged. The difficulty is then to describe the behavior of such an object. On the one hand, all those positive charges repel each other (in the same fashion as the '+' side of two magnets next to each other), but on the other hand, the bag keeps them together with the rest of the marbles. Protons and neutrons even go beyond this analogy, for they also have the strange habit of pairing with each other.

In addition to all these effects, the bag is not rigid and can be deformed into non-spherical shapes : squeezed like a rugby ball, or flattened like a pancake. Describing the atomic nucleus properly requires taking into account all of these features. This leads to a problem : solving exactly the equations that rule these interactions involves mathematical techniques that take a lot of computing power. As a result we usually approximate these equations, which raises a new question : how does one do that, and how can we judge the validity of such an approximation ?

One answer (among many) is given in this thesis where we consider one estimate, called the Pairing-Plus-Quadrupole model. We try to enhance it using new formulas in combination with the work of two scientists, K. Kumar and B. Sørensen. The aim here is to propose an approximation that will bring results with a satisfactory level of precision and which will be easy and fast to run on a computer.

The atomic nucleus is the heart of matter and is widely used for many applications such as energy production, medical imaging with MRI or cancer treatment. As a consequence, an efficient description of nuclei is very useful and can help unveiling their full potential.

Résumé populaire

Un étrange sac plein d'étranges billes

La matière est constituée d'atomes, eux-mêmes constitués de particules chargées, appelées électrons, qui orbitent autour d'un noyau massif. Ce noyau est lui-même constitué de deux types de particules : les protons et les neutrons. Les neutrons sont électriquement neutres, à l'inverse des protons qui sont positivement chargés. On peut alors imaginer le noyau comme un sac rempli de billes, certaines neutres, d'autres chargées. Décrire le comportement d'un tel objet devient alors difficile. D'une part, toutes les billes chargées se repoussent les unes des autres (comme le font les pôles Sud de deux aimants), et d'autre part, le sac les confine avec les autres billes. Les protons et les neutrons dépassent en fait cette analogie puisqu'ils ont en plus l'étrange habitude de s'apparier.

De plus, le sac n'est pas rigide. Il peut ainsi se déformer et ne plus être sphérique, en s'allongeant comme un ballon de rugby, ou en s'aplatissant comme un frisbee. Pour décrire le noyau correctement, il est alors nécessaire de tenir compte de tous ces phénomènes, créant ainsi le problème suivant : résoudre exactement les équations qui régissent ces interactions demande une grande puissance de calcul. On approxime donc ces équations pour les rendre plus simple, ce qui soulève une nouvelle question : comment faire, et comment s'assurer de la validité de ces approximations ?

Une réponse possible (parmi de nombreuses autres) est apportée par cette étude. On considère ici un modèle appelé "Pairing-Plus-Quadrupole" que l'on tente d'améliorer en combinant de nouvelles formules et le travail de deux physiciens, K. Kumar et B. Sørensen. Le but de ce mémoire est donc de proposer une approximation qui nous permette d'obtenir des résultats satisfaisants, et qui soit facile à calculer avec un ordinateur.

Le noyau atomique est le cœur de la matière et la compréhension de sa structure est utile dans bien des domaines : production d'énergie, imagerie médicale par IRM, ou encore traitement contre le cancer. Une description efficace du noyau présente donc un grand intérêt et permettra de révéler tout le potentiel de ce dernier.